Electrical source imaging of interictal spikes using multiple sparse volumetric priors for presurgical epileptogenic focus...

Article *in* NeuroImage: Clinical · January 2016

DOI: 10.1016/j.nicl.2016.01.017

CITATIONS
3

READS
78

10 authors, including:

Evelien Carrette
Universitair Ziekenhuis Ghent
41 PUBLICATIONS **470** CITATIONS
SEE PROFILE

Kristl Vonck
Ghent University
207 PUBLICATIONS **3,829** CITATIONS
SEE PROFILE

Stefaan Vandenberghe
Ghent University
224 PUBLICATIONS **2,024** CITATIONS
SEE PROFILE

Pieter Van Mierlo
Ghent University
63 PUBLICATIONS **185** CITATIONS
SEE PROFILE

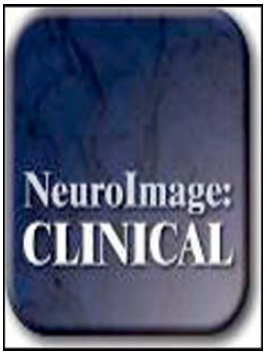

Electrical source imaging of interictal spikes using multiple sparse volumetric priors for presurgical epileptogenic focus localization

Gregor Strobbe, Evelien Carrette, José David López, Dirk Van Roost, Alfred Meurs, Kristl Vonck, Paul Boon, Stefaan Vandenberghe, Pieter van Mierlo

PII: S2213-1582(16)30013-4
DOI: doi: 10.1016/j.nicl.2016.01.017
Reference: YNICL 660

To appear in: *NeuroImage: Clinical*

Received date: 9 June 2015
Revised date: 9 October 2015
Accepted date: 17 January 2016

Please cite this article as: Strobbe, Gregor, Carrette, Evelien, López, José David, Van Roost, Dirk, Meurs, Alfred, Vonck, Kristl, Boon, Paul, Vandenberghe, Stefaan, van Mierlo, Pieter, Electrical source imaging of interictal spikes using multiple sparse volumetric priors for presurgical epileptogenic focus localization, *NeuroImage: Clinical* (2016), doi: 10.1016/j.nicl.2016.01.017

Electrical source imaging of interictal spikes using multiple sparse volumetric priors for presurgical epileptogenic focus localization

Gregor Strobbe[a,b,*], Evelien Carrette[c], José David López[e], Dirk Van Roost[d], Alfred Meurs[c], Kristl Vonck[c], Paul Boon[c], Stefaan Vandenberghe[a,b], Pieter van Mierlo[a,b]

[a] *Ghent University, Department of Electronics and Information Systems, MEDISIP, De Pintelaan 185, Building BB floor 5, 9000, Ghent, Belgium*
[b] *iMinds Medical IT department, Belgium*
[c] *Laboratory for Clinical and Experimental Neurophysiology, Ghent University Hospital, Ghent, Belgium*
[d] *Department of Neurosurgery, Ghent University Hospital, Ghent, Belgium*
[e] *SISTEMIC, Department of Electronic Engineering, Universidad de Antioquia UDEA. Calle 70 No. 52-21,Medellín, Colombia*
[f] *Catholic University College of Bruges-Ostend, Faculty of Engineering Technology, Electronics/ICT, Zeedijk 101, 8400, Ostend, Belgium*

Abstract

Electrical source imaging of interictal spikes observed in EEG recordings of patients with refractory epilepsy provides useful information to localize the epileptogenic focus during the presurgical evaluation. However, the selection of the time points or time epochs of the spikes in order to estimate the origin of the activity remains a challenge. In this study, we consider a Bayesian EEG

*Corresponding author - phone number: +32484777651
Email addresses: gregor.strobbe@ugent.be (Gregor Strobbe), evelien.carrette@ugent.be (Evelien Carrette), josedavid@udea.edu.co (José David López), dirk.vanroost@ugent.be (Dirk Van Roost), alfred.meurs@ugent.be (Alfred Meurs), kristl.vonck@ugent.be (Kristl Vonck), paul.boon@uzgent.be (Paul Boon), stefaan.vandenberghe@ugent.bfe (Stefaan Vandenberghe), pieter.vanmierlo@ugent.be (Pieter van Mierlo)

source imaging technique for distributed sources, i.e. the multiple volumetric sparse priors (MSVP) approach. The approach allows to estimate the time courses of the intensity of the sources corresponding with a specific time epoch of the spike. Based on presurgical averaged interictal spikes in six patients who were successfully treated with surgery, we estimated the time courses of the source intensities for three different time epochs: (i) an epoch starting 50 ms before the spike peak and ending at 50% of the spike peak during the rising phase of the spike, (ii) an epoch starting 50 ms before the spike peak and ending at the spike peak and (iii) an epoch containing the full spike time period starting 50 ms before the spike peak and ending 230 ms after the spike peak. To identify the primary source of the spike activity, the source with the maximum energy from 50 ms before the spike peak till 50% of the spike peak was subsequently selected for each of the time windows. For comparison, the activity at the spike peaks and at 50% of the peaks was localized using the LORETA inversion technique and an ECD approach. Both patient-specific spherical forward models and patient-specific 5-layered finite difference models were considered to evaluate the influence of the forward model. Based on the resected zones in each of the patients, extracted from post-operative MR images, we compared the distances to the resection border of the estimated activity. Using the spherical models, the distances to the resection border for the MSVP approach and each of the different time epochs were in the same range as the LORETA and ECD techniques. We found distances smaller than 23 mm, with robust results for all the patients. For the finite difference models, we found that the distances to the resection border for the MSVP inversions of the full spike

time epochs were generally smaller compared to the MSVP inversions of the time epochs before the spike peak. The results also suggest that the inversions using the finite difference models resulted in slightly smaller distances to the resection border compared to the spherical models. The results we obtained are promising because the MSVP approach allows to study the network of the estimated source-intensities and allows to characterize the spatial extent of the underlying sources.

Keywords: EEG, source priors, volumetric priors, Bayesian model selection, interictal spikes, ECD, LORETA

1. Introduction

Approximately 30% of the patients with epilepsy suffer from refractory epilepsy, a condition in which epileptic seizures are not adequately controlled with anti-epileptic drugs. One of the treatments for refractory epilepsy patients is epilepsy surgery (Boon et al., 1999b). The suitability for a surgical procedure to treat the patient is assessed during the presurgical evaluation. During this evaluation, different anatomical and functional techniques, investigating various aspects of the patient's epilepsy, are combined in order to delineate the zone that is responsible for initiating the seizures. This is the the so called epileptogenic zone (EZ), whose removal or disconnection is necessary for abolition of the seizures (Luders & Awad, 1992). The recording of the electroencephalogram (EEG) that measures the electrical brain activity non-invasively by means of electrode sensors placed on the patient's head, is one of the cornerstone techniques. EEG recordings allow to identify the seizure onset zone (SOZ), defined by the region in the brain generating the seizure onset discharges in the EEG, and the irritative zone (IZ) defined by the region in the brain generating interictal epileptiform discharges (IED) in the EEG in between the seizures (Rosenow & Lüders, 2001).

Interictal spikes are typical manifestations of IED in the EEG. They are characterized by a large amplitude rapid component lasting 50 - 100 ms that is usually followed by a slow wave, 200 - 500 ms in duration (de Curtis et al., 2012). Electrical source imaging (ESI) techniques allow to localize the generating sources of intertical spikes in order to delineate the IZ (Michel et al., 2004; Kaiboriboon et al., 2012; Michel & Murray, 2012). Several studies showed high positive predictive value of interictal spike ESI during the

presurgical evaluation (Boon et al., 1997a,b, 1999a; Michel et al., 1999; Plummer et al., 2007; Oliva et al., 2010; Brodbeck et al., 2010, 2011). However, the precise clinical value for epileptogenic focus localization is challenging because the IZ could be distant and, or completely separate from the SOZ and the EZ (Kaiboriboon et al., 2012). Moreover, the IZ is considered to be spatially more extensive than the SOZ (Carrette et al., 2011b).

The generation of interictal spikes is a complex phenomenon, and propagation of activity from the source to remote cortical regions can occur within milliseconds (Alarcon et al., 1994; Wennberg et al., 2011; Kaiboriboon et al., 2012). As a consequence, a common problem in the ESI procedure is the selection of the time points or time epochs of the spike in order to localize the primary sources of the activity and not the areas to which the epileptic activity is spreading. It has been shown in previous studies that the early component of the spike is likely to represent the location and field of the source, and the peak of the epileptiform discharge actually reflects propagated activity (Merlet et al., 1996; Lantz et al., 2003; Rose & Ebersole, 2009; Plummer et al., 2008; Aydin et al., 2015). As such, modeling of the spike peak could be misleading to delineate the IZ. However, the early component of the spike is of much smaller amplitude compared to the peak, so accurate modeling may be easily affected by noise contamination (Scherg et al., 1999).

The golden standard to assess the accuracy of ESI for interictal spikes is to compare the results of ESI with (simultaneously) recorded spikes from intracranial EEG. These kind of datasets are however restricted for validation to the locations where the intracranial electrodes are placed. Moreover, simultaneous recordings will affect the ESI results due to skull defects and

the placement of the electrodes (Li et al., 2007; Lanfer et al., 2012, 2013; Lau et al., 2014). An alternative way is to evaluate presurgical EEG data with a high incidence of interictal spikes that were recorded in patients with good surgical outcome and who showed no interictal spike activity in postsurgical EEG registrations. Studies show that areas with high incidence of interictal spikes highly correlate with the EZ (Asano et al., 2003; Marsh et al., 2010) and the resection of the IZ, instead of the EZ provides good surgical outcome (Bautista et al., 1999). Moreover, a study using simultaneously recorded EEG/MEG and intracranial recordings showed that the very early components of interictal spike activity were not yet subject to propagation and were found within the SOZ (Aydin et al., 2015). By including these kind of patients and retrospectively analyzing interictal epileptiform spikes, the ESI activity can be correlated to the resected zone (Mégevand et al., 2014). This relies on the assumption that the very early components of the interictal spike activity in these patients, which are not necessarily visible in the EEG, were part of the EZ.

In this paper we evaluate an ESI technique that allows to estimate the activity of sources distributed in the brain of the patient corresponding with a specific time epoch of the interictal spike activity. It is an application of our previous work in which we suggested to use multiple sparse volumetric priors (MSVP) for ESI using the hierarchical Bayesian framework implemented in the statistical parametric mapping software [1] (Strobbe et al., 2014a,b). Compared to the more traditional approaches, where the sources are typi-

[1] A MATLAB (The mathworks. Inc., Natick, USA) toolbox for the analysis of EEG, MEG, PET, SPECT and fMRI data

cally estimated that correspond to the spike peak, or to 50% of the spike peak during the rising phase of the spike (Boon et al., 1997a, 1999a; Brodbeck et al., 2011; Birot et al., 2014), the choice of the time epoch in order to localize the origin of the activity using the MSVP method is not clear. In the Ossa et al. (2015) study, the authors already suggested to use the approach by limiting the inversion procedure to a specific time epoch before the spike. In this study, three different time epochs were chosen for inversion: (i) a window starting 50 ms before the spike peak and ending at 50% of the spike peak during the rising phase of the spike, (ii) a window starting 50 ms before the spike peak and ending at the spike peak and (iii) a window starting 50 ms before the spike peak and ending 230 ms after the spike peak. For each of the time windows, the time courses of the intensity of the distributed sources in the brain of the patients were estimated. Subsequently, the primary sources generating the interictal spikes were identified as the sources with the maximum energy corresponding to the beginning of the spike till 50% of the peak during the rising phase of the spike.

For verification, we compared the performance of the MSVP approach with the results obtained with the LORETA approach and an equivalent current dipole (ECD) approach. For these more traditional approaches we estimated the sources at the spike peak and at 50% of the spike peak during the rising phase of the spike. Based on interictal spikes recorded in six patients that were rendered seizure free after surgery and that showed no interictal spikes in post-operative routine EEG recordings, we were able to evaluate the considered approaches by comparing the distances of the estimated activity to the border of the resected area.

2. Patient data

We retrospectively selected interictal spike data in six patients with refractory partial temporal lobe epilepsy who underwent resective surgery using the following inclusion criteria: (i) the patient was seizure free (i.e. Engel class I) after surgery, with minimum follow up of 1.5 years, (ii) the electrode positions were known, (iii) the seizures and the majority of interictal spikes showed the same lateralization in the EEG recordings, i.e. over the left or right hemisphere and (iv) there were no spikes observed in routine EEG registrations of 0.5 hour, 6 months after resection. An overview of the patient data is given in tables 1 and 2.

Three patients had 27 channel EEG recordings and 3 patients had 64 channel EEG recordings. The recorded interictal EEG data was first filtered between 0.5 and 40 Hz with a Butterworth zero phase filter and a 50 Hz notch filter implemented in the Brain Vision Analyzer software (Brainproducts, Munich). Spike selection was visually performed by one expert electrophysiologist (AM or EC) experienced in reading clinical EEG. All patients had one dominant spike type with an invariable morphology and maximal amplitude at the same electrode. For patient 2 both anterior and posterior spikes were observed over the left hemisphere. The majority of spikes were anterior and selected for analysis. For the patients that showed bilateral interictal activity, i.e. patient 3 and 5, we only selected the dominant side for analysis because more than 90% of the spikes originated from that side. The spikes were marked at the time point with the highest amplitude, i.e. the peak of the spike, on the same channel. The spikes were subsequently segmented from -50 ms to 230 ms around the peak, in order to include the large

patient	1	2	3
sex	F	F	F
age (surgery)	18	25	39
epilepsy type	TLE	TLE	TLE
#electrodes	61 (64)	61 (64)	62 (64)
elec. pos.	Digitizer	Digitizer	Digitizer
removed elec.	FC1, FC2, C3	FC1, FC2, C3	P1 , C3
samping freq.	1023.87 Hz	1023.87 Hz	1023.87 Hz
visual inspection scalp EEG	right frontotemporal spikes + ictal discharges over right hemisphere	left frontotemporal spikes + ictal discharges over left hemisphere	right frontotemporal spikes + ictal discharges over the right frontotemporal region
#spikes (avg)	15	12	31
abundance spikes	100% Right	100% Left (anterior, posterior)	>90% Right
phase rev.	T8	T7	F8
MRI	right hippocampal sclerosis	left hippocampal sclerosis	right hippocampal sclerosis
surgery	right selective amygdalohippocampectomy	left selective amygdalohippocampectomy	right anterior 2/3 temporal lobectomy incl. hippocampectomy
resection vol.	2.7 cm^3	5.3 cm^3	27.7 cm^3
follow up	3 years	3.5 years	1.5 year
Engel class	Class 1	Class 1 (1 aura)	Class 1 (aura's)
spikes post-op routine EEG	no	no	no

Table 1: Overview of the patient data, P1-3, we used in this study. The total number of electrodes was 64, but some of them were removed because of bad signal quality. F = Female, TLE = Temporal Lobe Epilepsy, phase rev. = phase reversal, elec. pos. = electrode positions, sampling freq. = sampling frequency, resection vol. = resection volume, post-op = post operative

patient	4	5	6
sex	F	F	F
age (surgery)	41	26	64
epilepsy type	TLE	TLE	TLE
#electrodes	27	26 (27)	27
elec. pos.	CT	CT	CT
removed elec.	/	O1	/
samping freq.	128 Hz	256 Hz	128 Hz
visual inspection scalp EEG	left frontotemporal spikes + ictal discharges over the left frontotemporal region	right frontotemporal spikes + bilateral frontotemporal ictal discharges	left frontotemporal spikes + ictal discharges over the left frontotemporal region
#spikes (avg)	35	41	14
abundance spikes	100 % Left	> 90% right	100% Left
phase rev.	F7	F8	F7
MRI	left hippocampal sclerosis	dysplastic lesion in right gyrus temporalis inferior	lesion in amygdala gyrus parahippocampalis
surgery	left selective amygdalohippocampectomy	right anterior 2/3 temporal lobectomy	left selective amygdalohippocampectomy
resection vol.	4.7 cm^3	32.7 cm^3	6.1 cm^3
follow up	3 years	4 years	4 years
Engel class	Class 1	Class 1	Class 1
spikes post-op routine EEG	no	1 (on 10 routine EEGs)	no

Table 2: Overview of the patient data, P4-6 we used in this study. The total number of electrodes was 27, but some of them were removed because of bad signal quality. F = Female, TLE = Temporal Lobe Epilepsy, phase rev. = phase reversal, elec. pos. = electrode positions, sampling freq. = sampling frequency, resection vol. = resection volume, post-op = post operative

amplitude rapid component followed by a slow wave for inversion. The spikes were subsequently averaged. Some electrodes were removed in the analysis due to bad signal quality. In Figs. 1 and 2, the averaged spikes for the 64 channel and 27 channel recordings are shown, respectively. The electrode for spike selection and the number of averaged spikes are depicted for each patient. For each of the patients the topography corresponding to the spike peak and at 50% of the peak is also shown. The spikes were finally average referenced before ESI.

Figure 1: The averaged spikes and topographies corresponding with the spike peak and at 50% of the spike peak for the 64 channels recordings in patient 1 to 3. The vertical blue lines correspond with the spike peaks. The vertical dashed lines correspond with 50% of the spike peak during the rising phase of the peak. The channel to select the peak of the spike and the number of spikes that were averaged are given for each patient.

Figure 2: The averaged spikes and topographies corresponding with the spike peak and at 50% of the spike peak for the 27 channels recordings in patient 4 to 6. The vertical dashed lines correspond with 50% of the spike peak during the rising phase of the peak. The channel to select the peak of the spike and the number of spikes that were averaged are given for each patient.

For all patients, presurgical and postsurgical anatomical MR images were available. We manually segmented the resected zone from the postsurgical anatomical MR images to determine the volume of the resection and to compare the ESI approaches considered in this study. We extracted the electrode

positions from CT images of the patients (with scalp electrodes attached) for the 27 channel recordings and Polhemus recordings (by Polhemus Inc., USA) for the 64 channel EEG.

3. EEG source imaging of interictal spikes

The MSVP technique is compared to two approaches typically used in clinical practice: an equivalent current dipole (ECD) approach (Scherg, 1990) and the low resolution electromagnetic tomography algorithm known as LORETA (Pascual-Marqui et al., 1994).

For each of these inversion techniques we considered two types of forward models. We used the CARTOOL software (by Denis Brunet (brainmapping.unige.ch/cartool)) to construct patient-specific spherical forward models for all patients. In addition, 5-layered patient-specific models were constructed based on the finite difference method (FDM)(Hallez et al., 2005; Strobbe et al., 2014a) in order to investigate the effect of using more advanced forward models. In what follows we provide the details of the considered approaches.

3.1. Forward modeling

3.1.1. Locally Spherical Model with Anatomical Constraints (LSMAC)

In the CARTOOL software, multi-layer spherical head models were constructed taking into account the anatomical presurgical MR images of the patients. This approach is known as the Locally Spherical Model with Anatomical Constraints, or LSMAC model (Brunet et al., 2011; Birot et al., 2014). In this approach, an adaptive local spherical model is used at each electrode.

To do so, the thicknesses of the scalp, skull and brain are estimated from the MR images of the patients. These thicknesses are then used in a 3-shell spherical model with the local radiuses. Around 5000 dipole solution points with free orientations were distributed with mean inter-dipole distances of approximately 3 mm inside the brain surface for each patient. The lead field matrices in x, y and z directions were subsequently computed for each electrode using the known analytical solutions for a three-shell spherical head model (Ary et al., 1981).

3.1.2. Finite difference modelling

For each patient, FDM head models were constructed based on the presurgical anatomical MR images of the patients. Nested meshes representing the scalp, outer skull and inner skull were extracted from the MR images in SPM. These meshes were subsequently converted to volumes. We segmented gray matter, white matter and CSF using Freesurfer segmentation techniques (Fischl, 2012). Based on these segmentations and the inner volumes that were built from the surface meshes, 5-layered head models were constructed including scalp, skull, gray and white matter and CSF layers. The conductivity of the CSF was set to 1.79 S/m (Baumann et al., 1997), 0.33 S/m for gray matter, 0.14 S/m for white matter, 0.022 S/m and 0.33 S/m for the skull and scalp, respectively (Montes-Restrepo et al., 2014; Vorwerk et al., 2014). The resulting volumetric head models were resampled to $1 \times 1 \times 1$ mm voxel resolution.

For each of the head models, the source space was constructed based on the segmented gray matter. The dipoles were assumed inside the gray matter (excluding the cerebellum) on a cubic grid equidistant to each other with a 1

mm spacing. We ensured that at least 2 voxels of gray matter were between the central node of the dipole model and the boundaries with other tissues in the x, y and z directions. This resulted in approximately 10,000 dipoles inside the gray matter for each of the models. We subsequently subsampled the dipole source space with a spacing of 3 mm resulting in approximately 2,000 dipoles inside the gray matter for each model.

3.2. Inverse modeling

3.3. ECD and LORETA

The details of the ECD modelling technique can be found in (Scherg, 1990). For the LORETA solutions we used the CARTOOL software for the LSMAC forward models and an in-house approach for the FDM models. The details of the LORETA approach can be found in (Pascual-Marqui et al., 1994).

3.3.1. Multiple sparse volumetric priors

In the multiple sparse volumetric priors approach, multiple active regions in the brain can be introduced as priors before inversion in order to estimate the intensity of multiple sources that are distributed in the brain of the patient. Each region is modeled as a covariance component that can be introduced to model the prior variance of a specific area in the brain based on the idea that an area that is modeled with a high variance is more likely to be active. After introducing the priors, the intensities of the dipoles in the distributed source model are estimated using a variational Bayesian scheme by optimizing the free energy cost function. The mathematical details of the MSVP approach are explained in Appendix A. We applied the MSVP

technique using the LSMAC forward models and the finite difference forward models.

LSMAC models

For each of the considered dipoles in the source space, 3 different covariance components corresponding with the x, y and z-direction, were introduced for inversion. For each of the covariance components, only the diagonal element corresponding with the index of that specific dipole was considered to be different from zero. As such no information about the neighbourhood of the dipole was included. This approach can be seen as a multiple dipole model for which every dipole has the same likelihood to be active.

Finite difference forward models

In order to apply the MSVP technique, the orientations of the dipoles were determined based on the curvature of the segmented white matter (see Phillips et al. (2002) and Strobbe et al. (2014b) for more details). Based on the dipole source space in each patient, we constructed 100 possible sets of 256 sparse volumetric regions.

For each set of volumetric regions, we assured global gray matter coverage by randomly selecting 1 dipole seed from all possible locations in 256 fixed gray matter volumes covering the full gray matter. For each of the dipole seeds a region was subsequently grown inside the gray matter of the patient (Strobbe et al., 2014b). The maximum distance to the original dipole and the smoothing factor were set to 5 mm and 0.6, respectively. Each of the regions was subsequently introduced as a single predefined covariance matrix. As such, 256 covariance matrices were introduced as priors for inversion.

The most likely set of the 100 possible sets of volumetric regions was

finally selected based on Bayesian model selection using the free energy values corresponding with each of the inversions, see Appendix A.3.

3.4. Comparison of the ESI approaches

For all the ESI approaches considered in this study, we calculated the distances to the resected zone (d_r), defined as the closest distance of the estimated activity to the resection border, which is illustrated in Fig. 5. For the ECD approach, we calculated the d_r for the dipole source corresponding with the spike peak and at 50% of the spike peak. For the LORETA approach we calculated the d_r based on the dipole source with the maximum estimated activity corresponding with the spike peak and at 50% of the spike peak. For the MSVP approach, the time courses of all the dipoles were estimated corresponding with tree different windows: (i) a window starting before the spike peak and ending at 50% of the spike peak during the rising phase of the spike, (ii) a window starting before the spike peak and ending at the spike peak and (iii) a window starting 50 ms before the spike peak and ending 230 ms after the spike peak. Subsequently, the source with the maximum estimated energy from -50 ms to 50% of the spike peak during the rising phase of the spike was selected and d_r was calculated for each of the different time windows. The same amount of prior variance was assumed on all electrodes.

4. Results

4.1. Overall results

4.1.1. LSMAC forward models

The d_r values for each method are shown in Fig. 4. Overall, the mean and standard deviation of 7.1 $\pm$ 6.0 mm for the d_r based on the LORETA

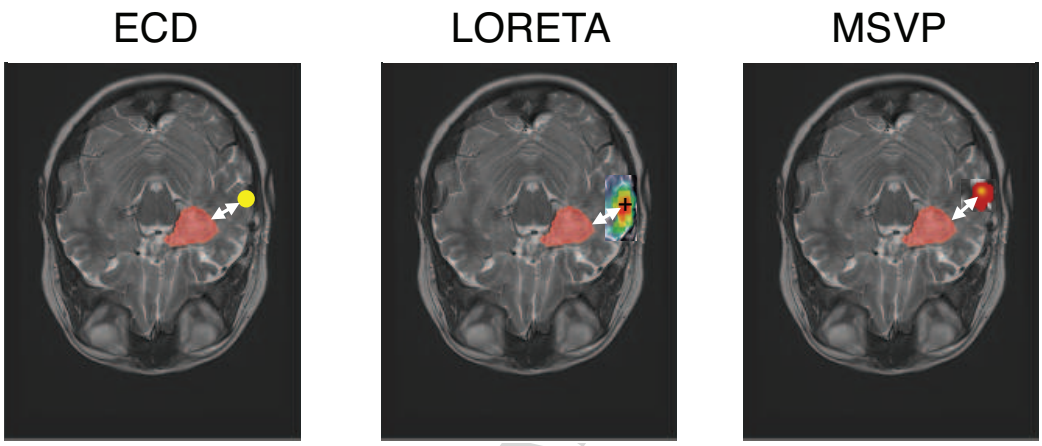

Figure 3: Illustration of the distance to the border of the resection for each of the considered approaches. For the LORETA and MSVP approaches, the maximum estimated intensity of the dipole in the distributed source model is used to calculate the distance.

approach at the peak of the spikes were the smallest. For the LORETA approach at 50% of the spike peak we found 12.5 ± 11.0 mm. For the MSVP method using the time window from -50 ms to 50% of the spike peak, from -50ms to the spike peak and using the full spike time window, we found 11.4 ± 7.1 mm, 14.1 ± 11.2 mm and 11.6 ± 7.0 mm, respectively. For the ECD solutions we found 10.2 ± 6.6 mm at 50% of the spike peak, and 8.5 ± 6.4 mm at the spike peak.

In one patient, the proposed MSVP method, using the time window from -50ms to the peak, estimated the maximum activity inside the resected zone, compared to two patients using LORETA at the spike peak.

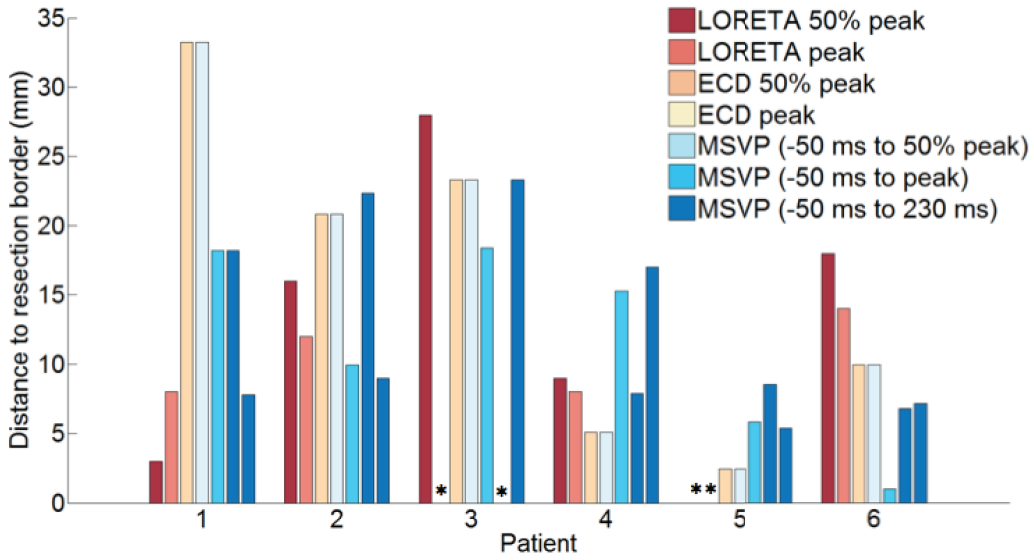

	Distance to resection border (mm)						
	LORETA 50% peak	LORETA peak	ECD 50% peak	ECD peak	MSVP (-50 ms to 50% peak)	MSVP (-50 ms to peak)	MSVP (-50 ms to 230ms)
mean	12.5	7.1	15.8	15.8	11.4	10.6	11.6
std	11.0	6.0	11.9	11.9	7.1	8.2	7.0

Figure 4: The distance to the resection border, d_r (in mm) for each of the patients (P1 to P6) and for the different inversion methods. In the table below, the means and standard deviations of each method are given. The stars denote the situations in which the activity was correctly estimated inside the resected area

4.1.2. Finite difference forward models

The d_r values for the LORETA, ECD and MSVP approach using the finite different methods are shown in Fig. 5. Overall, the mean and standard deviation of 3.8 ± 5.1 mm for the d_r based on the proposed MSVP method using the full spike time course were the smallest distances to the border of the resection. For the MSVP method using smaller time windows, i.e. from -50 ms to 50% of the spike peak and from -50ms to the spike peak, we found 10.8 ± 9.3 mm and 14.1 ± 11.2 mm, respectively. The mean and standard deviation of d_r based on LORETA were 12.5 ± 11.0 mm at 50% of the spike peak and 7.1 ± 6.0 mm at the spike peak. For the ECD solutions we found 10.2 ± 6.6 mm at 50% of the spike peak, and 8.5 ± 6.4 mm at the spike peak.

In three patients, the proposed MSVP method using the full spike time course estimated the maximum activity inside the resected zone, compared to two patients using the MSVP method based on a window cropped to the rising phase of the spike. Using the LORETA approach, the maximum activity was estimated inside the resected zone for one patient at 50% of the spike and for two patients at the spike peak. For the ECD approach the activity was estimated inside the resected zone for one patient at 50% of the spike peak and at the spike peak.

The overall maximum distance to the resection of the MSVP approach using the full spike time course was 12 mm compared to 14 mm and 24 mm for the LORETA solutions at 50% of the spike peak and at the spike peak, respectively, 16 mm and 15 mm for the ECD solution at 50% of the spike peak and on the spike peak, respectively, and 23 mm and 23 mm for the

MSVP approaches based on a window cropped to the rising phase of the spike.

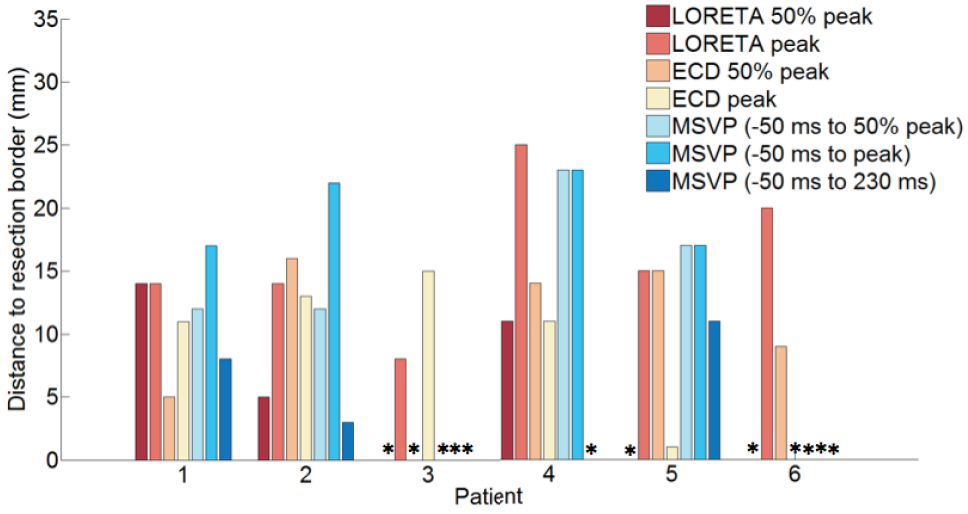

	Distance to resection border (mm)						
	LORETA 50% peak	LORETA peak	ECD 50% peak	ECD peak	MSVP (-50 ms to 50% peak)	MSVP (-50 ms to peak)	MSVP (-50 ms to 230ms)
mean	5.0	16.0	9.8	8.5	10.7	13.1	3.7
std	6.2	5.8	6.4	6.4	9.2	10.8	4.8

Figure 5: The distance to the resection border, d_r (in mm) for each of the patients (P1 to P6) and for the different methods. In the table below, the means and standard deviations of each method are given. The stars denote the situations in which the activity was correctly estimated inside the resected area

4.1.3. Comparison of the forward modelling approaches

In Fig. 6 we compared the distances to the resection border of the LORETA, ECD and MSVP approaches using the LSMAC and FDM forward models respectively. For 4 of the 7 approaches, i.e. the LORETA approach at 50%

of the peak, both ECD approaches and the MSVP using the full spike time window, the FDM forward models resulted in smaller distances to the resection border. Only for the LORETA approach at the peak of the spike we found that the LSMAC models resulted in smaller distances to the resection border. For the other MSVP cases there was no clear difference.

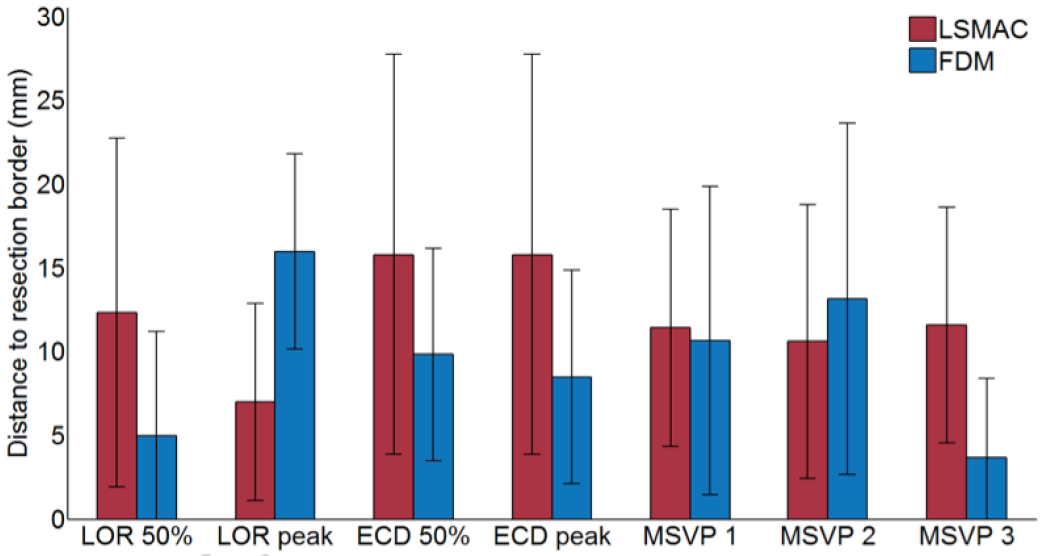

Figure 6: Comparison of the distances to the border of the resection for the LORETA, ECD and MSVP approaches using the LSMAC and FDM forward models respectively. LOR 50%: LORETA at 50% of the peak, LOR peak: LORETA at the peak, MSVP 1: MSVP (-50ms to 50% peak), MSVP 2: MSVP (-50ms to peak), MSVP 3: MSVP (-50ms to 230 ms). The error bars denote the standard deviation over the 6 patients.

4.2. Individual patient results

The results of patient 1 are presented in Fig. 7. In the first row we show the resection in horizonal slices. The ESI results are shown table-wise below.

The rows represent the inversion approaches and the columns the forward modelling approaches. For each of the methods we show the activity in three orthogonal slices on top of the post-operative MR image. For the LORETA approach, we show the 95 percentile of the activity corresponding with the activity at 50% of the spikes peak during the rising phase of the spike. The slice indices correspond with the location of the maximum estimated activity. For the ECD and MSVP solutions the location of the estimated sources are also shown on top of the post-operative MR image. To select the slices, we used the average location of the estimated sources.

The results of the MSVP approach corresponding to the full spike time window and the finite difference forward models are presented in Fig. 8. In subfigure A, a histogram depicts the number of reconstructions, corresponding to a certain free energy value, for different sets of MSVPs. We selected the set of volumetric regions corresponding with the highest free energy for further analysis in subfigure B. In subfigure B, we show the evoked energy (from -50 ms to 50% of the spike peak) for the estimated time courses of the estimated dipoles. The sources with the highest energy are depicted by S1, S2, S3 and S4. In subfigure C, the time courses of the sources are shown. The dipole with the highest energy in a time window from -50 ms to 50% of the spike peak is depicted by S1 and its location and region extent is shown on top of the post-operative MR image in subfigure D. The results for the MSVP approach using the other time windows and for the LSMAC forward models were generated equivalently.

All the results for the other patients can be found in Supplementary Materials and are presented in the same fashion.

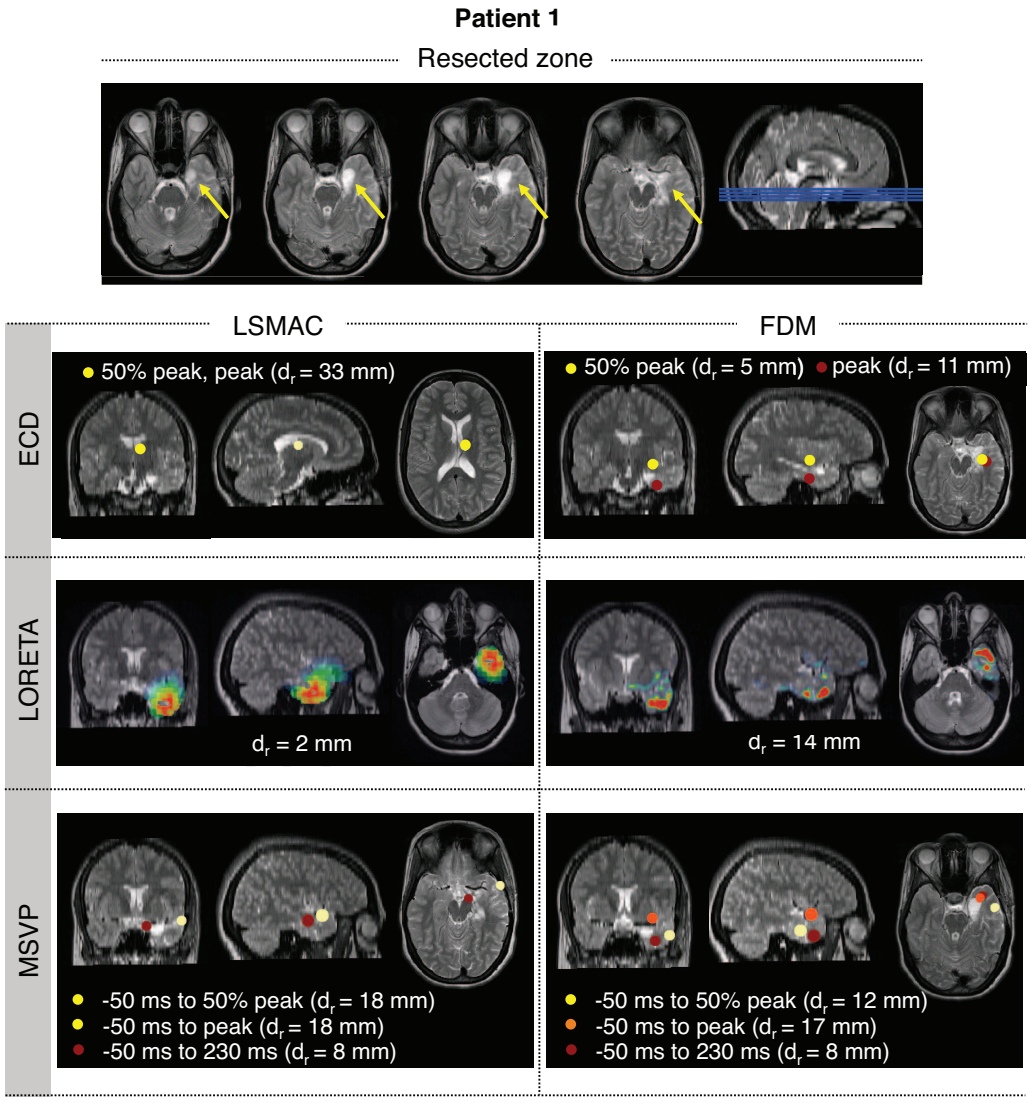

Figure 7: First row: illustration of the resected zone of patient 1 in different horizontal slices. The results below are depicted by the rows corresponding with the inversion approaches and the columns representing the forward models. For the LORETA approaches the results are shown corresponding with the activity at 50% of the peak of the spike.

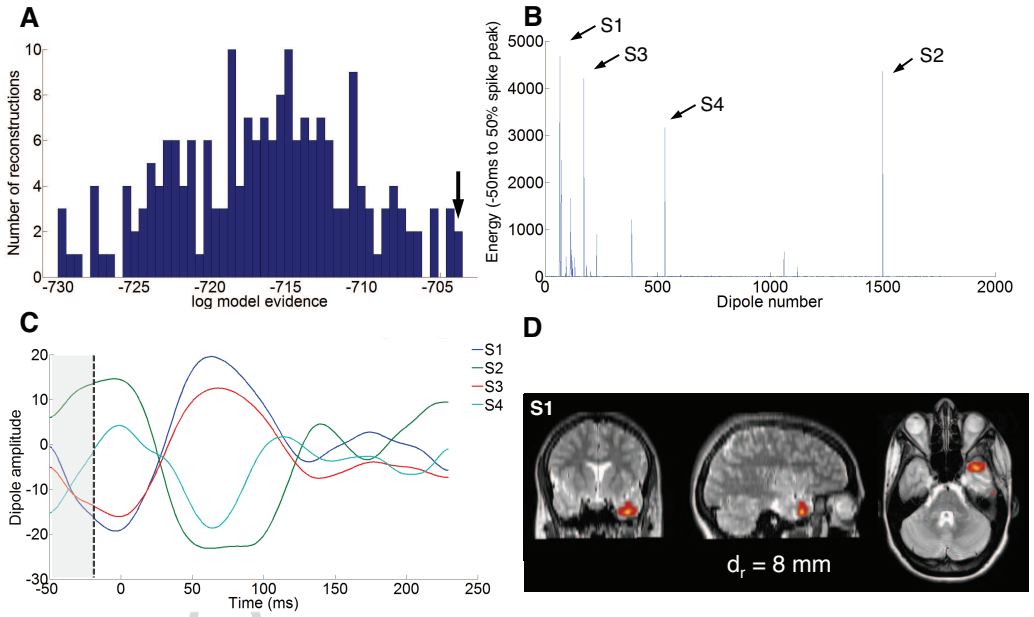

Figure 8: Panel A: histogram of the free energy values corresponding with the with the MSVP inversions. Panel B: energy of the dipole intensities based on the MSVP solution. The dipoles with the maximum energy are depicted by S1, S2, S3 and S4. Panel C: the time courses of S1, S2, S3 and S4. Panel D: the location of volumetric region shown on top of the resected zone in 3 orthogonal slices corresponding with S1.

5. Discussion

This paper demonstrates a hierarchical Bayesian ESI approach to estimate the sources generating interictal spike activity in scalp EEG. The approach is based on the multiple sparse volumetric priors technique and uses a maximum energy criterium on the estimated dipole intensities, to identify the primary sources of the activity, i.e. the sources where the activity originated from. The localization results clearly corresponded to the resected zone in all patients. We compared the approach with the results of the LORETA approach and an ECD modelling technique. Overall, we found equally good or smaller distances to the resection border for both the spherical forward models and finite difference method models with robust results for all patients. We found that using the finite difference models, the distances to the resection border for the MSVP inversions and the full spike time periods were generally smaller compared to the MSVP inversions of the time periods before the spike peak. We did not observe clear trends for the LORETA and ECD approaches comparing the activity estimated at the spike peaks and at 50% of the spike peaks. The results suggest that the inversions using the finite difference models resulted in slightly smaller distances to the resection border compared to the spherical models.

For the LSMAC forward models we did not introduce volumetric regions as source priors. The LSMAC forward models consist of 3-layered spherical head models that do not incorporate the gray matter in the volume conductor model itself. As such it is not relevant to grow regions within a gray matter boundary because this could lead to model misconceptions. For simplicity and comparison purposes with the other considered techniques we therefore

chose to introduce each dipole as a separate prior.

This study can be compared to other recent studies that showed the potential of Bayesian approaches using a distributed source model to estimate the underlying sources of interictal activity (Heers et al., 2014, 2015). In these studies, the authors chose to use the whole time window for spike inversion. Here, we evaluated the influence of using smaller time windows before the spike. The reason to use smaller time windows before the spike was to evaluate the algorithm in conditions where it was not forced to reduce the error for the peak activity and thereby ignoring the activity of interest. We found that the choice of the time window clearly affected the location of the region with the highest energy, which is similar to the findings reported in (Lantz et al., 2003). For the finite difference forward models, we found that the distances to the resection border for the MSVP inversions of the time epochs before the spike were generally higher compared to the MSVP inversions of the full spike time period. We assume that this observation is due to increasing noise levels in the beginning of the rising phase of the spike. In order to investigate this more in depth, more patients are needed.

As stated in the introduction, we assumed that the very early phases of the interictal spike activity originated inside the resected tissue and the activity then propagated to adjacent regions in the temporal cortex to generate clearly observable spike activity in the EEG. Note that the resection of tissue can therefore lead to the disappearance of spikes in postsurgical EEG, even if the location of the interictal spike, as observed in presurgical EEG, is in unremoved tissue. Because of propagation of the interictal spike activity to the neighboring areas in the brain, we have to be careful to use the resection

border to evaluate the different methods. Especially for patients 1, 2, 4 and 6 who underwent a left or right selective amygdalohippocampectomy caution is warranted. Discharges in the hippocampus or amygdala are assumed to produce no observable scalp EEG rhythms (Pacia & Ebersole, 1997; Jan et al., 2010; Yamazaki et al., 2012). The interictal spike activity observed in the EEG is caused by adjacent regions in the temporal cortex because of spreading from the hippocampus or amygdala as was shown in (Zumsteg et al., 2006) and (Merlet et al., 1998; Carrette et al., 2011a; Koessler et al., 2015). Patients 3 and 5 had a 2/3 anterior temporal lobectomy. In these patients the resected zone was larger. For patients 3 and using the finite difference forward models, all the approaches estimated the activity inside the resected zone except the LORETA approach at 50% of the spike peak and the ECD approach at the peak of the spike. For patient 5, only the LORETA approach estimated the activity inside the resected zone, both at 50% of the spike peak and at the spike peak for the spherical forward models and at 50% of the spike peak for the finite difference forward models. In order to estimate the IZ more precisely, (simultaneous) intracranial recordings are necessary. These were however not available for all the patients in this study.

So far many studies in EEG source imaging for presurgical focus localisation used ECD models (Boon et al., 1997a; Ebersole, 2000; Ebersole & Ebersole, 2010; Wennberg & Cheyne, 2014). The ECD model is limited because it does not allow to investigate the spatial extent of the sources corresponding with the interictal activity because the ECD only represents the center of mass of the generators of interictal activity. Since combined EEG with in-

tracranial EEG and MEG with intracranial EEG studies have demonstrated that extended areas should be at least 6 to 10 cm^2 of synchronously active cortex to produce IEDs in EEG recordings (Mikuni et al., 1997; Lantz et al., 2003; Tao et al., 2005; von Ellenrieder et al., 2014) we have to be aware of the fact that a point source, like an ECD, that models such an extended source must be deeper in the brain than the actual generating cortex (Ebersole & Ebersole, 2010; Koessler et al., 2015).

Recent studies proposed techniques such as the maximum entropy on the mean (MEM), similar to MSVP, and ExSO-music to estimate the spatial extent of the sources that generate EEG signals (Chowdhury et al., 2013; Birot et al., 2011; Becker et al., 2014). Especially in the (Heers et al., 2015) study, it was shown very elegantly that the MEM method was capable of estimating the spatial extent of the sources generating interictal spike activity. In order to be sensitive to the spatial extent of the sources in a hierarchical Bayesian framework, Chowdhury et al. (2013) suggested to use regions with a size that was larger than the size of the expected sources. Since the area of the sources should be at least 6 to 10 cm^2, we chose to set the parameters of the region growing and the smoothness factor for the MSVP approach using the finite difference models, in such a way that the volume of the regions was approximately 3 by 3 by 3 mm. The choice of these parameters will influence the extent of the estimated activity. The thorough investigation of these settings was not within the scope of this study.

A set of volumetric priors was constructed for the MSVP approach using the finite difference models by randomly selecting 1 dipole seed from each of the 256 different fixed regions in the gray matter of the patient to cover

the whole gray matter layer. Different numbers could also have been evaluated but we do not expect much differences in the results since (Chowdhury et al., 2013) showed that the MEM framework was able to estimate simulated sources whatever the number and size of the regions were defining the inversion model. A smaller number of volumetric regions would result in smaller sampling of the gray matter and higher numbers would increase the complexity of the problem. Using the MSVP technique, each of the priors is weighted based on the data by estimating the hyperparameters, so the most relevant priors are selected for any set of priors anyway. A thorough evaluation of the size and number of regions was outside the scope of this study. Moreover, regions constructed based on (f)MRI prior knowledge, clinical results from PET or SPECT studies of the patients, etc. can easily be introduced in the MSVP framework. Afterwards it can be evaluated whether the results improve with additional prior knowledge using Bayesian model selection.

Note that we only selected the solution with the highest free energy to compare the estimated activity based on the MSVP approach with finite difference forward models. In some cases there were inversions with similar free energy values near the highest free energy value. For these solutions we calculated the Bayesian Model Average (BMA) in an interval of 3 from the highest free energy (Trujillo-Barreto et al., 2004; Lopez et al., 2012). The BMA approach did however not influence the selection of the source location with the maximum activity and therefore did not influence the findings based on the results corresponding with the maximum free energy.

An important factor influencing the ESI results is the choice of the forward model for the ECD, LORETA and MSVP technique. In this work we used

both spherical and 5-layered patient specific head models. Moreover, we used both free and fixed orientations of the dipoles. Although the work of (Birot et al., 2014) suggests there is no need for highly sophisticated head models in clinical applications, the results in this study indicate that the more realistic FDM forward model may result in smaller distances to the resection border. In order to validate this, more patients are needed and the results should be verified with intracranial EEG recordings to clearly delineate the IZ.

There are some issues that we did not address in this paper. For example the time window around the spike peak we used for inversion, i.e. -50 ms to 230 ms, could be chosen differently. In general, it is important to include the rising phase (from -50 ms to the peak) of the spike in order to include the origin of the epileptic activity (Lantz et al., 2003; Rose & Ebersole, 2009; Plummer et al., 2008). Moreover, for the LORETA and ECD approaches, we only evaluated the results corresponding with the peaks of the spikes and at 50% of the peaks. More time points could have been shown but we did not include this in the study because of small localization differences or bad ECD fitting due to increasing noise levels in the beginning of the rising phase of the spike. We only evaluated averaged spikes for inversion because the ECD solutions for single spikes were highly sensitive to noise. Finally, we analyzed both 27-channel and 64-channel EEG data but did not evaluate the effect of using a different number of electrodes because of the small patient group and the small differences we found between the distance to the resection. There are many opportunities for future work. First of all network effects can be studied based on the estimated time courses of the dipoles. This can be investigated in future studies using different techniques

than the energy criterium that was suggested here, to estimate connectivity patterns between the sources, for example using dynamic causal modeling (Lemieux et al., 2011) or functional connectivity approaches (van Mierlo et al., 2014). Moreover, it is important in future studies to evaluate the applicability of ESI techniques in order to localize seizure activity. In this context, it is also important to focus on the network aspects of the estimated activity of the sources in order to localize the origin of the activity (Ding et al., 2007; Lu et al., 2012).

6. Conclusion

In this article, we presented an ESI technique to localize interictal spike activity based on patient specific head models and by introducing multiple volumetric sparse regions in a hierarchical Bayesian framework for distributed sources. The technique uses a specific time-window of the interictal spike activity to estimate the time courses of the intensity of the sources and subsequently selects the primary sources using a maximum energy criterium on the estimated source intensities during the rising phase of the spike. Based on averaged interictal spike data in six patients, the findings suggest that our approach is potentially useful to delineate the IZ in addition to other distributed approaches such as LORETA and the ECD model. In addition, the findings suggest that it is potentially useful to use 5-layered forward models compared to 3-layered spherical forward models.

7. Acknowledgements

J.D. López was financed by Convocatoria de sostenibilidad 2014-2015, CODI Universidad de Antioquia. The Cartool software has been programmed by Denis Brunet (brainmapping.unige.ch/cartool), from the Functional Brain Mapping Laboratory, Geneva, Switzerland, and is supported by the Center for Biomedical Imaging (CIBM) of Geneva and Lausanne.

8. Supplementary material

Appendix A. Hierarchical Bayesian source estimation

We can express the problem of EEG source imaging using a distributed source model in the context of a two-level hierarchical Bayesian model (Phillips et al., 2005):

$$\begin{aligned} V &= LJ + \epsilon_1 \\ J &= \epsilon_2 \end{aligned} \tag{A.1}$$

where $V \in \mathbb{R}^{N_c \times N_t}$ is the EEG dataset with N_c channels and N_t time samples, $J \in \mathbb{R}^{N_d \times N_t}$ the amplitude of N_d current dipoles at fixed locations and with fixed orientations, $L \in \mathbb{R}^{N_c \times N_d}$ is the lead field matrix linking the source amplitudes in J to the electrical scalp potentials in V and ϵ_1 and ϵ_2, the measurement and model uncertainty, both assumed to follow a Gaussian distribution with zero mean: $\epsilon_1 \sim N(0, C_\epsilon)$ and $\epsilon_2 \sim N(0, C_J)$. The covariance matrices C_e and C_J can be modeled as a linear combination of covariance components (Phillips et al., 2007):

$$\begin{aligned} C_\epsilon &= \lambda_1^{(1)} Q_1^{(1)} + \lambda_2^{(1)} Q_2^{(1)} + \cdots + \lambda_{N_e}^{(1)} Q_{N_c}^{(2)} \\ C_J &= \lambda_1^{(2)} Q_1^{(2)} + \lambda_2^{(2)} Q_2^{(2)} + \cdots + \lambda_{N_r}^{(2)} Q_{N_r}^{(2)} \end{aligned} \tag{A.2}$$

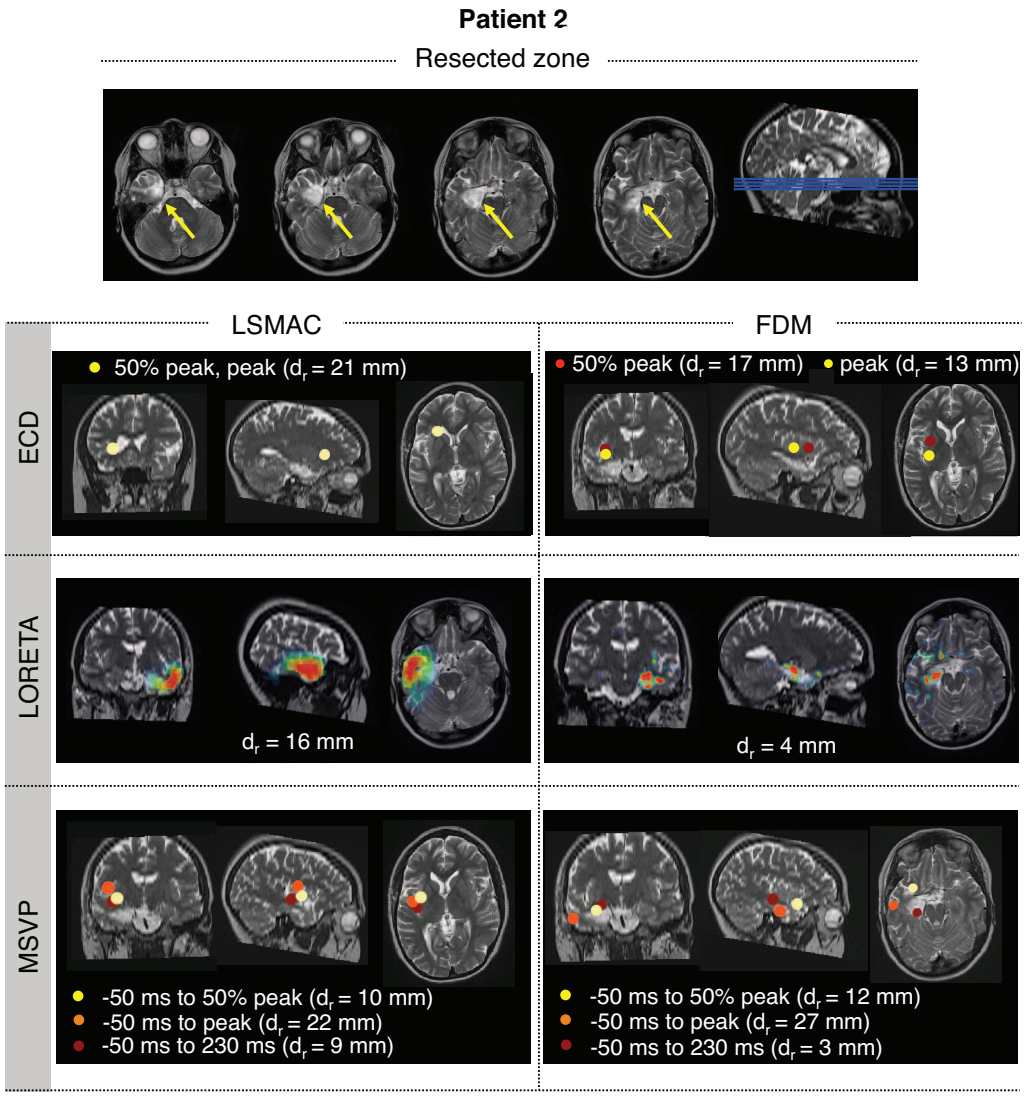

Figure 9: First row: illustration of the resected zone of patient 2 in different horizontal slices. The results below are depicted by the rows corresponding with the inversion approaches and the columns representing the forward models. For the LORETA approaches the results are shown corresponding with the activity at 50% of the peak of the spike.

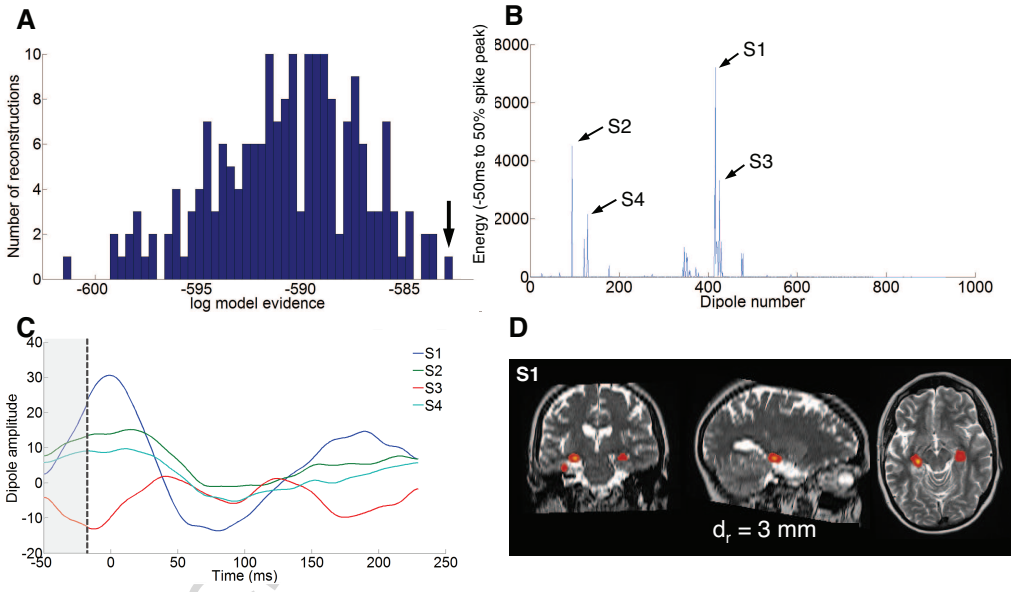

Figure 10: Panel A: histogram of the free energy values corresponding with the with the MSVP inversions of patient 2. Panel B: energy of the dipole intensities based on the MSVP solution. The dipoles with the maximum energy are depicted by S1, S2, S3 and S4. Panel C: the time courses of S1, S2, S3 and S4. Panel D: the location of volumetric region shown on top of the resected zone in 3 orthogonal slices corresponding with S1.

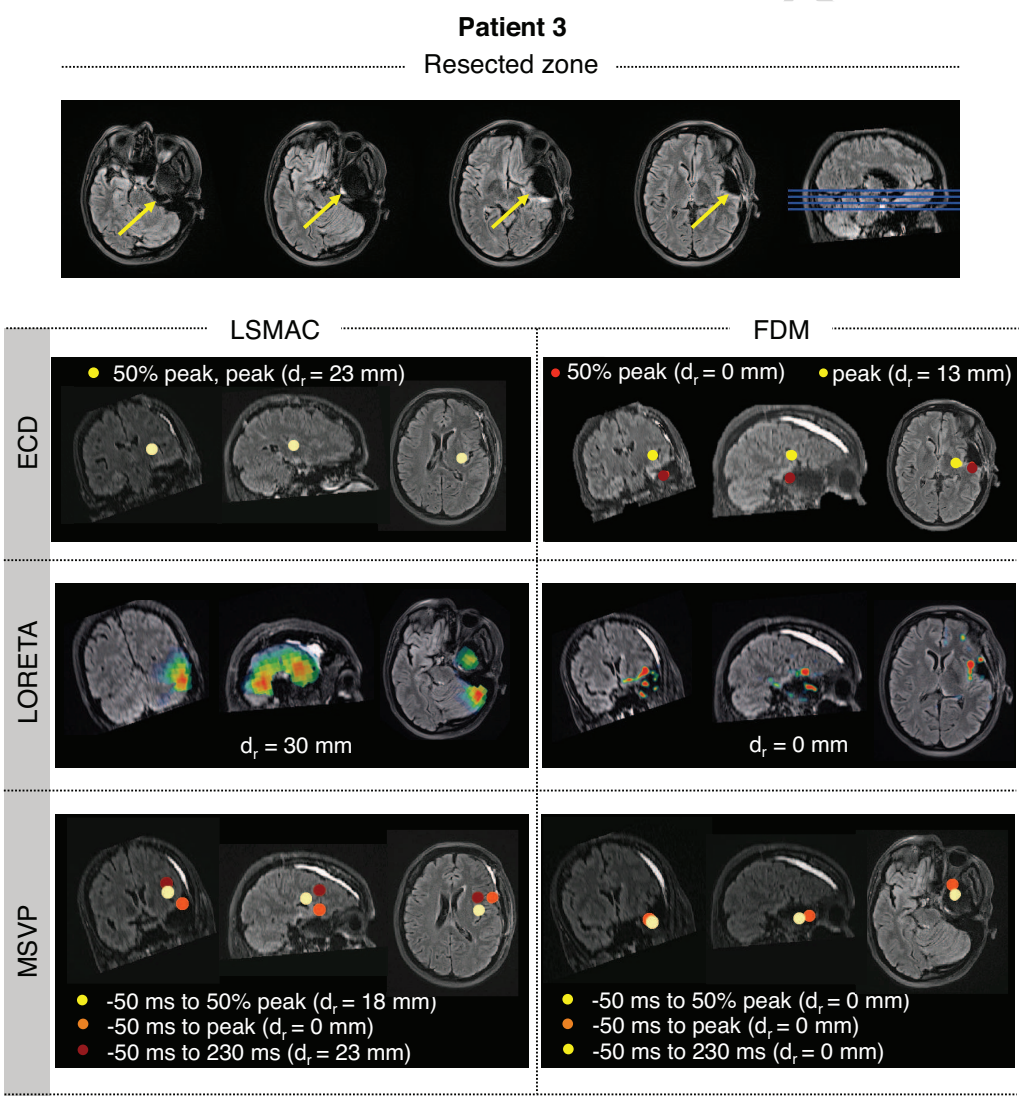

Figure 11: First row: illustration of the resected zone of patient 3 in different horizontal slices. The results below are depicted by the rows corresponding with the inversion approaches and the columns representing the forward models. For the LORETA approaches the results are shown corresponding with the activity at 50% of the peak of the spike.

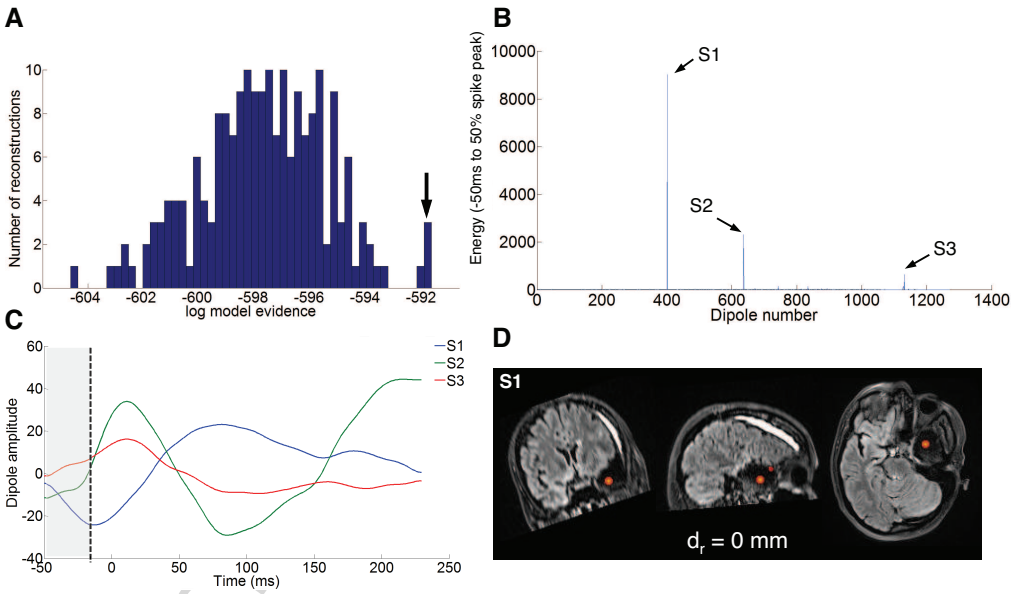

Figure 12: Panel A: histogram of the free energy values corresponding with the with the MSVP inversions of patient 3. Panel B: energy of the dipole intensities based on the MSVP solution. The dipoles with the maximum energy are depicted by S1, S2 and S3. Panel C: the time courses of S1, S2 and S3. Panel D: the location of volumetric region shown on top of the resected zone in 3 orthogonal slices corresponding with S1.

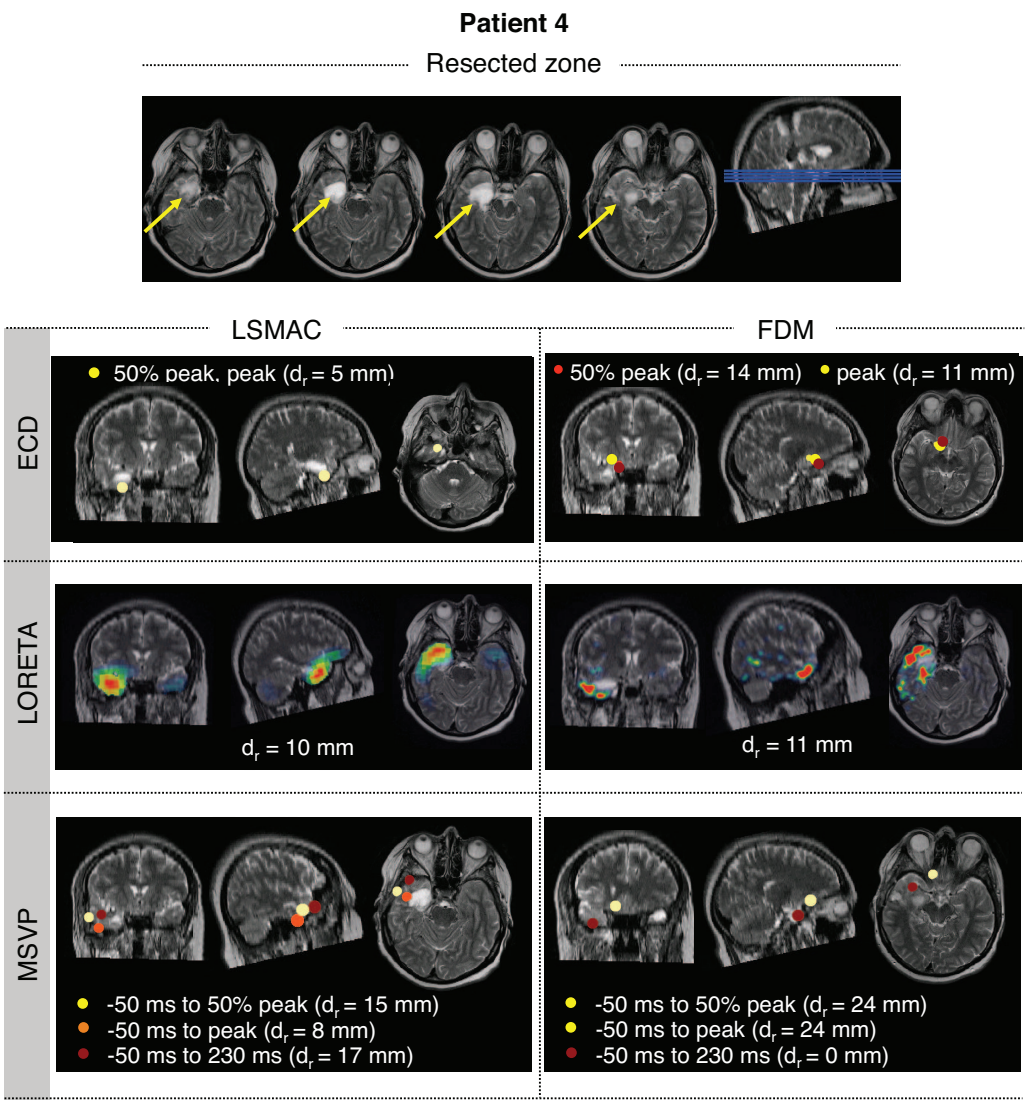

Figure 13: First row: illustration of the resected zone of patient 4 in different horizontal slices. The results below are depicted by the rows corresponding with the inversion approaches and the columns representing the forward models. For the LORETA approaches the results are shown corresponding with the activity at 50% of the peak of the spike.

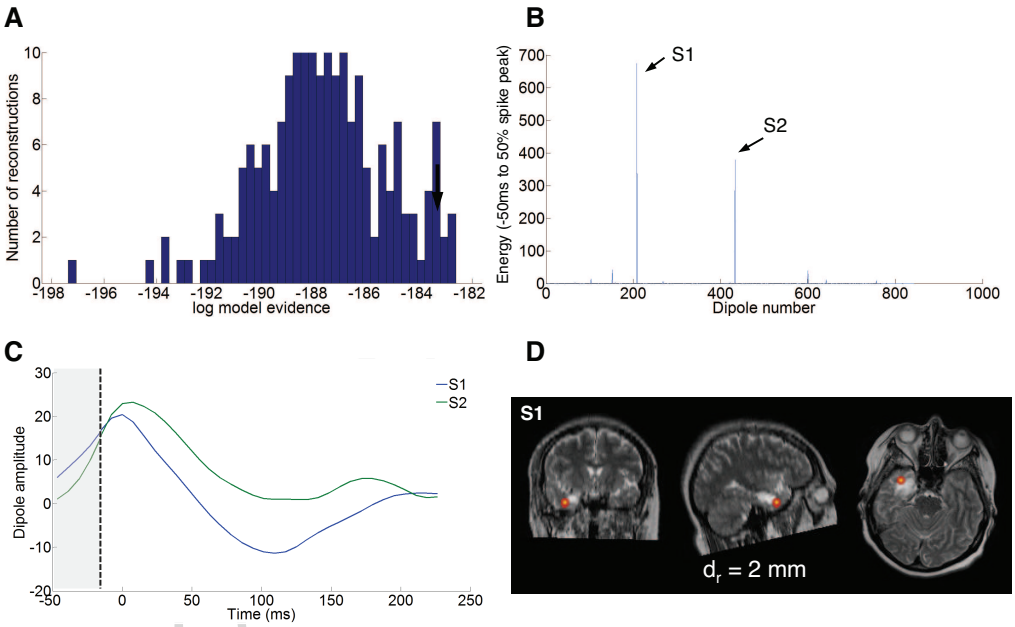

Figure 14: Panel A: histogram of the free energy values corresponding with the with the MSVP inversions of patient 4. Panel B: energy of the dipole intensities based on the MSVP solution. The dipoles with the maximum energy are depicted by S1 and S2. Panel C: the time courses of S1 and S2. Panel D: the location of volumetric region shown on top of the resected zone in 3 orthogonal slices corresponding with S1.

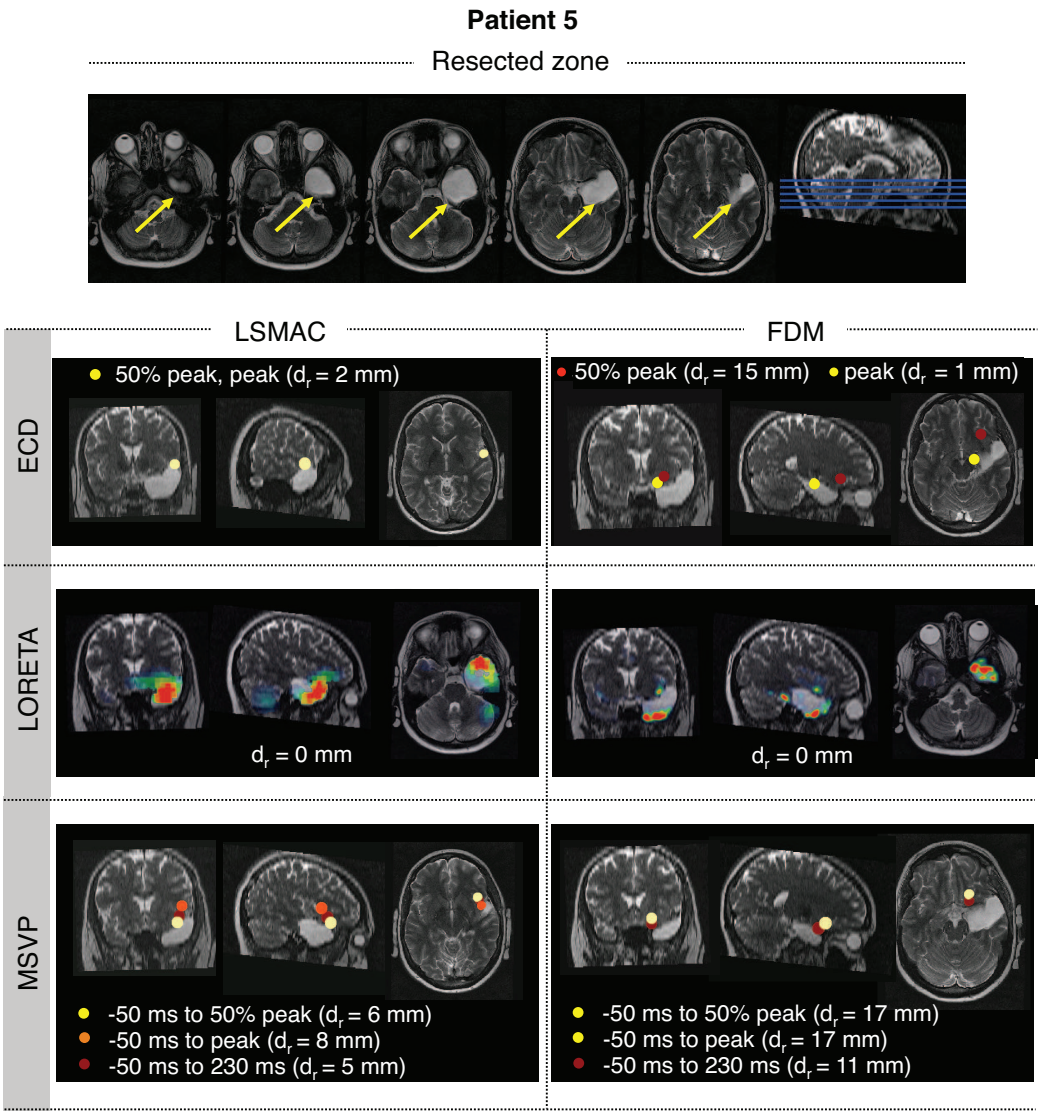

Figure 15: First row: illustration of the resected zone of patient 5 in different horizontal slices. The results below are depicted by the rows corresponding with the inversion approaches and the columns representing the forward models. For the LORETA approaches the results are shown corresponding with the activity at 50% of the peak of the spike.

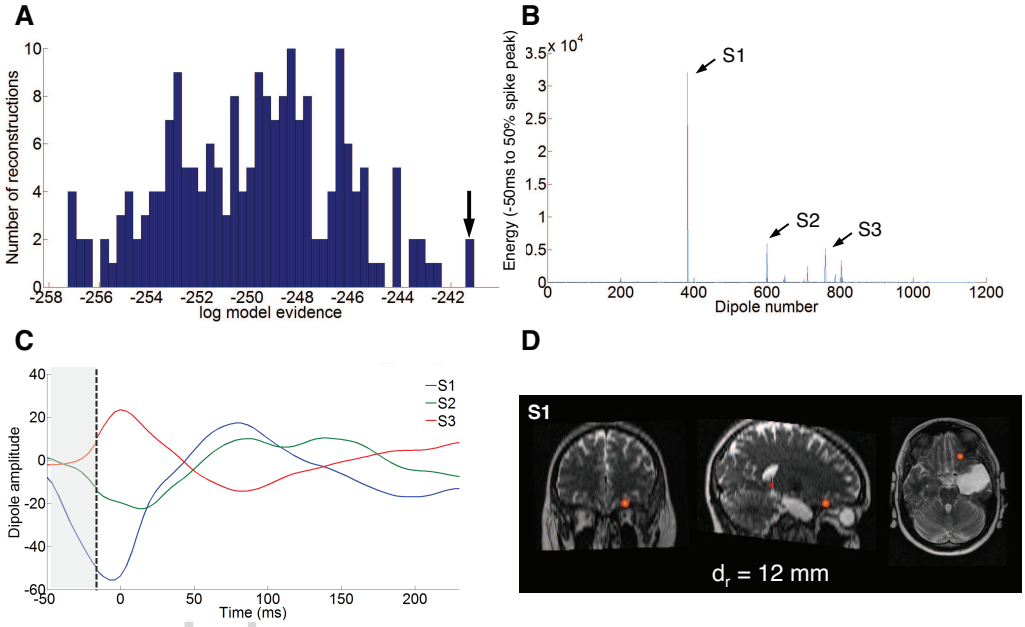

Figure 16: Panel A: histogram of the free energy values corresponding with the with the MSVP inversions of patient 5. Panel B: energy of the dipole intensities based on the MSVP solution. The dipoles with the maximum energy are depicted by S1, S2 and S3 Panel C: the time courses of S1, S2 and S3. Panel D: the location of volumetric region shown on top of the resected zone in 3 orthogonal slices corresponding with S1.

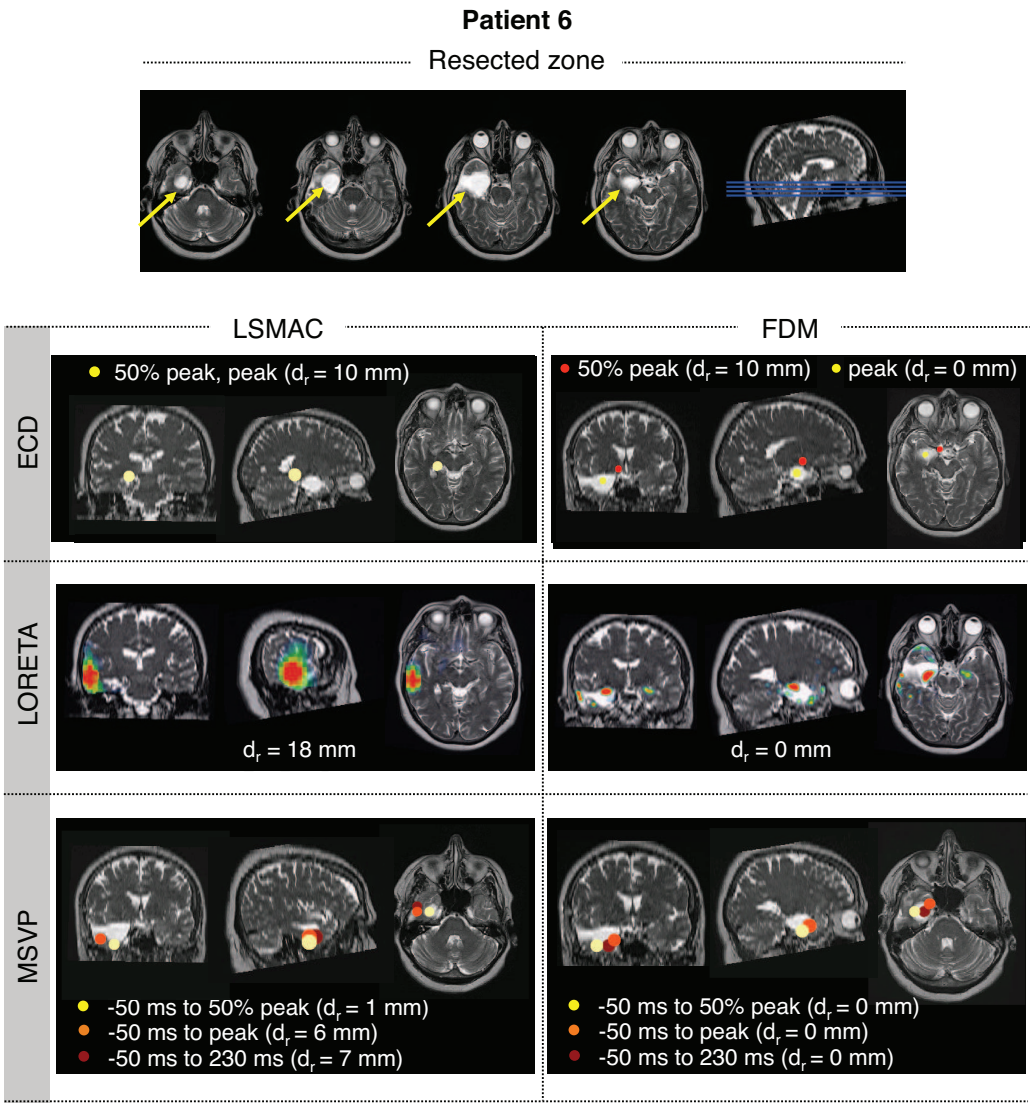

Figure 17: First row: illustration of the resected zone of patient 6 in different horizontal slices. The results below are depicted by the rows corresponding with the inversion approaches and the columns representing the forward models. For the LORETA approaches the results are shown corresponding with the activity at 50% of the peak of the spike.

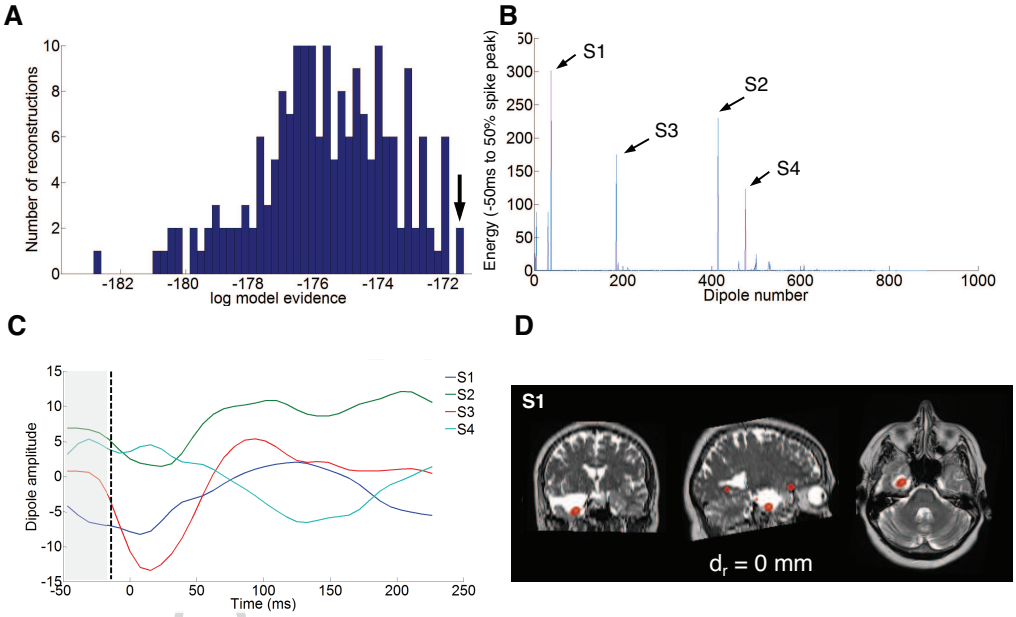

Figure 18: Panel A: histogram of the free energy values corresponding with the with the MSVP inversions. Panel B: energy of the dipole intensities based on the MSVP solution. The dipoles with the maximum energy are depicted by S1, S2, S3 and S4. Panel C: the time courses of S1, S2, S3 and S4. Panel D: the location of volumetric region shown on top of the resected zone in 3 orthogonal slices corresponding with S1.

Where $\lambda_1^{(1)}, \lambda_2^{(1)}, \ldots, \lambda_{N_e}^{(1)}$ and $\lambda_1^{(2)}, \lambda_2^{(2)}, \ldots, \lambda_{N_r}^{(2)}$ are the hyperparameters that balance the various covariance components either at the level of the electrodes containing N_e components or at the source level containing N_r components (Phillips et al., 2005). This framework is implemented in the statistical parametric mapping software SPM, in which the hyperparameters are estimated using a variational Bayesian estimation scheme. They are computed by optimizing the free energy cost function given the covariance components and data V (Friston et al., 2007). As such, $C_\epsilon(\mu_1)$ and $C_J(\mu_2)$, with $\mu_1 = \left\{\lambda_i^{(1)}\right\}$ with $i = 1, 2, \ldots, N_e$ and $\mu_2 = \left\{\lambda_i^{(2)}\right\}$ with $i = 1, 2, \ldots, N_r$, can be calculated. It follows that the expectation of the source intensities J given V is equal to:

$$E[p(J|V)] = C_J(\mu_2)L^T[LC_J(\mu_2)L^T + C_\epsilon(\mu_1)]^{-1}V \tag{A.3}$$

with $E[p(J|V)]$ the expected value of J given the measurements V.

Appendix A.1. Measurements covariance matrix

In absence of prior information, the same amount of prior variance on all electrodes is assumed: $C_\epsilon = \lambda_1^{(1)} I_{N_c}$, where $I_{N_c} \in \mathbb{R}^{N_c \times N_c}$ is an identity matrix, and $\lambda_1^{(1)}$ is the sensor noise variance. This means $N_e = 1$, and only one covariance component is assumed at the level of the electrodes.

Appendix A.2. Multiple Sparse Priors

A general approach is to consider multiple source priors as suggested in the multiple sparse priors (MSP) algorithm (Friston et al., 2008). Each covariance component in Eq. (A.2) can represent a potential activated area or active source in the brain of the patient. The hyperparameters $\lambda_i^{(2)}$, with

$i = 1, \ldots, N_r$, weight these covariance components and control the power allocated to each of them. The components may embody different types of informative priors, e.g. fMRI priors (Henson et al., 2011) or prior knowledge from other modalities such as PET or SPECT imaging.

In the multiple sparse priors (MSP) algorithm (Friston et al., 2008), N_q covariance components at the source level $Q = \left\{Q_1^{(2)}, \ldots, Q_{N_q}^{(2)}\right\}$ are assumed for which each of the components defines a potential activated region of cortex, with scalar hyperparameters, $\lambda = \left\{\lambda_i^{(2)}\right\}$, and $i = 1, \ldots, N_q$. Each covariance component is a diagonal matrix and the diagonal elements are constructed using the columns of the Green's function:

$$Q_G = \exp(\sigma G_L) \tag{A.4}$$

with σ a positive constant value that determines the smoothness of the current distribution or spatial extent of the activated regions, and $G_L \in \mathbb{R}^{N_d \times N_d}$, a graph Laplacian with inter-dipole connectivity information. The graph Laplacian G_L is calculated using an adjacency matrix corresponding with the dipole locations and defining the neighboring dipoles based on the dipole source space. Each column in the Green's function corresponds with a specific source assumed in the source space and models a patch or region on the cortex formed around that source. Each patch or region has a bell shape, with a full width half maximum depending on the neighboring dipoles and the smoothing factor σ:

Appendix A.3. Bayesian model selection based on free energy

The optimized free energy cost function to estimate the hyperparameters provides an upper bound on the Bayesian log evidence. This means the free

energy can be used to compared different models, including different sets of covariance components or introducing different forward modeling assumptions (Henson et al., 2009; Strobbe et al., 2014a,b). According to a decision rule described in Penny et al. (2004) one model can be chosen in favor of the other, when there is a difference in free energy (corresponding with reconstructions assuming each of the models) larger than 3.

Alarcon, G., Guy, C., Binnie, C., Walker, S., Elwes, R., & Polkey, C. (1994). Intracerebral propagation of interictal activity in partial epilepsy: implications for source localisation. *Journal of Neurology, Neurosurgery & Psychiatry*, *57*, 435–449.

Ary, J. P., Klein, S. A., & Fender, D. H. (1981). Location of sources of evoked scalp potentials: corrections for skull and scalp thicknesses. *Biomedical Engineering*, *28*, 447–52.

Asano, E., Muzik, O., Shah, A., Juhász, C., Chugani, D. C., Sood, S., Janisse, J., Ergun, E. L., Ahn-Ewing, J., Shen, C. et al. (2003). Quantitative interictal subdural eeg analyses in children with neocortical epilepsy. *Epilepsia*, *44*, 425–434.

Aydin, Ü., Vorwerk, J., Dümpelmann, M., Küpper, P., Kugel, H., Heers, M., Wellmer, J., Kellinghaus, C., Haueisen, J., Rampp, S. et al. (2015). Combined eeg/meg can outperform single modality eeg or meg source reconstruction in presurgical epilepsy diagnosis. *PloS one*, *10*, e0118753.

Baumann, S. B., Wozny, D. R., Kelly, S. K., & Meno, F. M. (1997). The Electrical Conductivity of Human Cerebrospinal Fluid at Body Temperature. *IEEE Trans Biomed Eng*, *44*, 220–223.

Bautista, R. E. D., Cobbs, M. A., Spencer, D. D., & Spencer, S. S. (1999). Prediction of surgical outcome by interictal epileptiform abnormalities during intracranial eeg monitoring in patients with extrahippocampal seizures. *Epilepsia*, *40*, 880–890.

Becker, H., Albera, L., Comon, P., Haardt, M., Birot, G., Wendling, F., Gavaret, M., Bénar, C.-G., & Merlet, I. (2014). Eeg extended source localization: tensor-based vs. conventional methods. *NeuroImage*, *96*, 143–157.

Birot, G., Albera, L., Wendling, F., & Merlet, I. (2011). Localization of extended brain sources from eeg/meg: the exso-music approach. *NeuroImage*, *56*, 102–113.

Birot, G., Spinelli, L., Vulliémoz, S., Mégevand, P., Brunet, D., Seeck, M., & Michel, C. M. (2014). Head model and electrical source imaging: A study of 38 epileptic patients. *NeuroImage: Clinical*, *5*, 77–83.

Boon, P., D'Havé, M., Adam, C., Vonck, K., Baulac, M., Vandekerckhove, T., & De Reuck, J. (1997a). Dipole modeling in epilepsy surgery candidates. *Epilepsia*, *38*, 208–18.

Boon, P., D'havé, M., Van Hoey, G., Vanrumste, B., Vonck, K., Adam, C., Vandekerckhove, T., Michielsen, G., Baulac, M., & De Reuck, J. (1999a).

Source localization in refractory partial epilepsy. *Revue neurologique*, *155*, 499–508.

Boon, P., D'Havé, M., Vandekerckhove, T., Achten, E., Adam, C., Clemenceau, S., Baulac, M., Goossens, L., Calliauw, L., & De Reuck, J. (1997b). Dipole modelling and intracranial EEG recording: correlation between dipole and ictal onset zone. *Acta neurochirurgica*, *139*, 643–52.

Boon, P., Vandekerckhove, T., Achten, E., Thiery, E., Goossens, L., Vonck, K., D'Have, M., Van Hoey, G., Vanrumste, B., Legros, B. et al. (1999b). Epilepsy surgery in belgium, the experience in gent. *Acta Neurologica Belgica*, *99*, 256–265.

Brodbeck, V., Spinelli, L., Lascano, A. M., Pollo, C., Schaller, K., Vargas, M. I., Wissmeyer, M., Michel, C. M., & Seeck, M. (2010). Electrical source imaging for presurgical focus localization in epilepsy patients with normal mri. *Epilepsia*, *51*, 583–591.

Brodbeck, V., Spinelli, L., Lascano, A. M., Wissmeier, M., Vargas, M.-I., Vulliemoz, S., Pollo, C., Schaller, K., Michel, C. M., & Seeck, M. (2011). Electroencephalographic source imaging: a prospective study of 152 operated epileptic patients. *Brain*, *134*, 2887–2897.

Brunet, D., Murray, M. M., & Michel, C. M. (2011). Spatiotemporal analysis of multichannel eeg: Cartool. *Computational intelligence and neuroscience*, *2011*, 2.

Carrette, E., de Beeck, M. O., Bourguignon, M., Boon, P., Vonck, K., Legros, B., Goldman, S., Van Bogaert, P., & De Tiege, X. (2011a). Recording

temporal lobe epileptic activity with meg in a light-weight magnetic shield. *Seizure*, *20*, 414–418.

Carrette, E., Vonck, K., & Boon, P. (2011b). The management of pharmacologically refractory epilepsy. *Int J Clin Rev*, *1*.

Chowdhury, R. A., Lina, J. M., Kobayashi, E., & Grova, C. (2013). Meg source localization of spatially extended generators of epileptic activity: comparing entropic and hierarchical bayesian approaches. *PLoS One*, *8*, e55969.

de Curtis, M., Jefferys, J. G., & Avoli, M. (2012). Interictal epileptiform discharges in partial epilepsy. *Jasper's Basic Mechanisms of the Epilepsies*, *80*, 213.

Ding, L., Worrell, G. A., Lagerlund, T. D., & He, B. (2007). Ictal source analysis: localization and imaging of causal interactions in humans. *Neuroimage*, *34*, 575–586.

Ebersole, J. S. (2000). Noninvasive localization of epileptogenic foci by eeg source modeling. *Epilepsia*, *41*, S24–S33.

Ebersole, J. S., & Ebersole, S. M. (2010). Combining meg and eeg source modeling in epilepsy evaluations. *Journal of Clinical Neurophysiology*, *27*, 360–371.

von Ellenrieder, N., Beltrachini, L., Perucca, P., & Gotman, J. (2014). Size of cortical generators of epileptic interictal events and visibility on scalp eeg. *Neuroimage*, *94*, 47–54.

Fischl, B. (2012). Freesurfer. *Neuroimage*, *62*, 774–781.

Friston, K., Harrison, L., Daunizeau, J., Kiebel, S., Phillips, C., Trujillo-Barreto, N., Henson, R., Flandin, G., & Mattout, J. (2008). Multiple sparse priors for the M/EEG inverse problem. *NeuroImage*, *39*, 1104–20.

Friston, K., Mattout, J., Trujillo-Barreto, N., Ashburner, J., & Penny, W. (2007). Variational free energy and the Laplace approximation. *NeuroImage*, *34*, 220–34.

Hallez, H., Vanrumste, B., Van Hese, P., D'Asseler, Y., Lemahieu, I., & Van de Walle, R. (2005). A finite difference method with reciprocity used to incorporate anisotropy in electroencephalogram dipole source localization. *Phys Med Biol*, *50*, 3787–3806.

Heers, M., Chowdhury, R. A., Hedrich, T., Dubeau, F., Hall, J. A., Lina, J.-M., Grova, C., & Kobayashi, E. (). Localization accuracy of distributed inverse solutions for electric and magnetic source imaging of interictal epileptic discharges in patients with focal epilepsy. *Brain Topography*, (pp. 1–20).

Heers, M., Chowdhury, R. A., Hedrich, T., Dubeau, F., Hall, J. A., Lina, J.-M., Grova, C., & Kobayashi, E. (2015). Localization accuracy of distributed inverse solutions for electric and magnetic source imaging of interictal epileptic discharges in patients with focal epilepsy. *Brain topography*, (pp. 1–20).

Heers, M., Hedrich, T., An, D., Dubeau, F., Gotman, J., Grova, C., & Kobayashi, E. (2014). Spatial correlation of hemodynamic changes related

to interictal epileptic discharges with electric and magnetic source imaging. *Human brain mapping*, *35*, 4396–4414.

Henson, R. N., Mouchlianitis, E., & Friston, K. J. (2009). MEG and EEG data fusion: Simultaneous localisation of face-evoked responses. *NeuroImage*, *47*, 581–589.

Henson, R. N., Wakeman, D. G., , V., Friston, K. J., & Trujillo-barreto, N. J. (2011). A parametric empirical Bayesian framework for the EEG / MEG inverse problem : generative models for multi-subject and multi-modal integration. *Front Hum Neurosci*, *5*, 1–16.

Jan, M. M., Sadler, M., & Rahey, S. R. (2010). Electroencephalographic features of temporal lobe epilepsy. *The Canadian Journal of Neurological Sciences*, *37*, 439–448.

Kaiboriboon, K., Lüders, H. O., Hamaneh, M., Turnbull, J., & Lhatoo, S. D. (2012). Eeg source imaging in epilepsypracticalities and pitfalls. *Nature Reviews Neurology*, *8*, 498–507.

Koessler, L., Cecchin, T., Colnat-Coulbois, S., Vignal, J.-P., Jonas, J., Vespignani, H., Ramantani, G., & Maillard, L. G. (2015). Catching the invisible: Mesial temporal source contribution to simultaneous eeg and seeg recordings. *Brain topography*, *28*, 5–20.

Lanfer, B., Röer, C., Scherg, M., Rampp, S., Kellinghaus, C., & Wolters, C. (2013). Influence of a silastic ecog grid on eeg/ecog based source analysis. *Brain topography*, *26*, 212–228.

Lanfer, B., Scherg, M., Dannhauer, M., Knösche, T. R., Burger, M., & Wolters, C. H. (2012). Influences of skull segmentation inaccuracies on eeg source analysis. *NeuroImage*, *62*, 418–431.

Lantz, G., Spinelli, L., Seeck, M., de Peralta Menendez, R. G., Sottas, C. C., & Michel, C. M. (2003). Propagation of interictal epileptiform activity can lead to erroneous source localizations: a 128-channel eeg mapping study. *Journal of clinical neurophysiology*, *20*, 311–319.

Lau, S., Flemming, L., & Haueisen, J. (2014). Magnetoencephalography signals are influenced by skull defects. *Clinical Neurophysiology*, *125*, 1653–1662.

Lemieux, L., Daunizeau, J., & Walker, M. C. (2011). Concepts of connectivity and human epileptic activity. *Frontiers in systems neuroscience*, *5*.

Li, J., Wang, K., Zhu, S., & He, B. (2007). Effects of holes on eeg forward solutions using a realistic geometry head model. *Journal of neural engineering*, *4*, 197.

Lopez, J. D., Espinosa, J. J., & Barnes, G. R. (2012). Random location of multiple sparse priors for solving the meg/eeg inverse problem. In *Engineering in Medicine and Biology Society (EMBC), 2012 Annual International Conference of the IEEE* (pp. 1534–1537). IEEE.

Lu, Y., Yang, L., Worrell, G. A., & He, B. (2012). Seizure source imaging by means of fine spatio-temporal dipole localization and directed transfer function in partial epilepsy patients. *Clinical Neurophysiology*, *123*, 1275–1283.

Luders, H., & Awad, I. (1992). Conceptual considerations. *Epilepsy surgery*, *1*, 51–62.

Marsh, E. D., Peltzer, B., Brown III, M. W., Wusthoff, C., Storm Jr, P. B., Litt, B., & Porter, B. E. (2010). Interictal eeg spikes identify the region of electrographic seizure onset in some, but not all, pediatric epilepsy patients. *Epilepsia*, *51*, 592–601.

Mégevand, P., Spinelli, L., Genetti, M., Brodbeck, V., Momjian, S., Schaller, K., Michel, C. M., Vulliemoz, S., & Seeck, M. (2014). Electric source imaging of interictal activity accurately localises the seizure onset zone. *Journal of Neurology, Neurosurgery & Psychiatry*, *85*, 38–43.

Merlet, I., Garcia-Larrea, L., Gregoire, M., Lavenne, F., & Mauguiere, F. (1996). Source propagation of interictal spikes in temporal lobe epilepsy. *Brain*, *119*, 377–392.

Merlet, I., Garcia-Larrea, L., Ryvlin, P., Isnard, J., Sindou, M., & Mauguiere, F. (1998). Topographical reliability of mesio-temporal sources of interictal spikes in temporal lobe epilepsy. *Electroencephalography and clinical neurophysiology*, *107*, 206–212.

Michel, C. M., & Murray, M. M. (2012). Towards the utilization of EEG as a brain imaging tool. *NeuroImage*, *61*, 371–385.

Michel, C. M., Murray, M. M., Lantz, G., Gonzalez, S., Spinelli, L., & Grave de Peralta, R. (2004). EEG source imaging. *Clin Neurophysiol*, *115*, 2195–222.

Michel, C. M., de Peralta, R. G., Lantz, G., Andino, S. G., Spinelli, L., Blanke, O., Landis, T., & Seeck, M. (1999). Spatiotemporal eeg analysis and distributed source estimation in presurgical epilepsy evaluation. *Journal of clinical neurophysiology*, *16*, 239–266.

van Mierlo, P., Papadopoulou, M., Carrette, E., Boon, P., Vandenberghe, S., Vonck, K., & Marinazzo, D. (2014). Functional brain connectivity from eeg in epilepsy: Seizure prediction and epileptogenic focus localization. *Progress in neurobiology*, *121*, 19–35.

Mikuni, N., Ikeda, A., Murao, K., Terada, K., Nakahara, I., Taki, W., Kikuchi, H., & Shibasaki, H. (1997). ?cavernous sinus eeg?: A new method for the preoperative evaluation of temporal lobe epilepsy. *Epilepsia*, *38*, 472–482.

Montes-Restrepo, V., van Mierlo, P., Strobbe, G., Staelens, S., Vandenberghe, S., & Hallez, H. (2014). Influence of skull modeling approaches on eeg source localization. *Brain topography*, *27*, 95–111.

Oliva, M., Meckes-Ferber, S., Roten, A., Desmond, P., Hicks, R. J., & OBrien, T. J. (2010). Eeg dipole source localization of interictal spikes in non-lesional tle with and without hippocampal sclerosis. *Epilepsy research*, *92*, 183–190.

Ossa, A., Borrego, C., Trujillo, M., & Lopez, J. D. (2015). Comparison of free distribution software for eeg focal epileptic source localization. In *Artificial Computation in Biology and Medicine* (pp. 368–376). Springer.

Pacia, S. V., & Ebersole, J. S. (1997). Intracranial eeg substrates of scalp ictal patterns from temporal lobe foci. *Epilepsia*, *38*, 642–654.

Pascual-Marqui, R. D., Michel, C. M., & Lehmann, D. (1994). Low resolution electromagnetic tomography: a new method for localizing electrical activity in the brain. *International journal of psychophysiology : official journal of the International Organization of Psychophysiology*, *18*, 49–65.

Penny, W. D., Stephan, K. E., Mechelli, a., & Friston, K. J. (2004). Comparing dynamic causal models. *NeuroImage*, *22*, 1157–72.

Phillips, C., Mattout, J., & Friston, K. J. (2007). *Statistical Paramteric Mapping*. Elsevier.

Phillips, C., Mattout, J., Rugg, M. D., Maquet, P., & Friston, K. J. (2005). An empirical Bayesian solution to the source reconstruction problem in EEG. *NeuroImage*, *24*, 997–1011.

Phillips, C., Rugg, M. D., & Friston, K. J. (2002). Anatomically informed basis functions for eeg source localization: combining functional and anatomical constraints. *NeuroImage*, *16*, 678–695.

Plummer, C., Harvey, A. S., & Cook, M. (2008). Eeg source localization in focal epilepsy: where are we now? *Epilepsia*, *49*, 201–218.

Plummer, C., Litewka, L., Farish, S., Harvey, A., & Cook, M. (2007). Clinical utility of current-generation dipole modelling of scalp eeg. *Clinical Neurophysiology*, *118*, 2344–2361.

Rose, S., & Ebersole, J. S. (2009). Advances in spike localization with eeg dipole modeling. *Clinical EEG and neuroscience*, *40*, 281–287.

Rosenow, F., & Lüders, H. (2001). Presurgical evaluation of epilepsy. *Brain*, *124*, 1683–1700.

Scherg, M. (1990). Fundamentals of dipole source potential analysis. *Auditory evoked magnetic fields and electric potentials. Advances in audiology*, *6*, 40–69.

Scherg, M., Bast, T., & Berg, P. (1999). Multiple source analysis of interictal spikes: goals, requirements, and clinical value. *Journal of Clinical Neurophysiology*, *16*, 214–224.

Strobbe, G., van Mierlo, P., De Vos, M., Mijović, B., Hallez, H., Van Huffel, S., López, J. D., & Vandenberghe, S. (2014a). Bayesian model selection of template forward models for eeg source reconstruction. *NeuroImage*, *93*, 11–22.

Strobbe, G., van Mierlo, P., De Vos, M., Mijović, B., Hallez, H., Van Huffel, S., López, J. D., & Vandenberghe, S. (2014b). Multiple sparse volumetric priors for distributed eeg source reconstruction. *NeuroImage*, *100*, 715–724.

Tao, J. X., Ray, A., Hawes-Ebersole, S., & Ebersole, J. S. (2005). Intracranial eeg substrates of scalp eeg interictal spikes. *Epilepsia*, *46*, 669–676.

Trujillo-Barreto, N. J., Aubert-Vázquez, E., & Valdés-Sosa, P. A. (2004). Bayesian model averaging in eeg/meg imaging. *NeuroImage*, *21*, 1300–1319.

Vorwerk, J., Cho, J.-H., Rampp, S., Hamer, H., Knösche, T. R., & Wolters, C. H. (2014). A guideline for head volume conductor modeling in eeg and meg. *NeuroImage*, .

Wennberg, R., & Cheyne, D. (2014). Eeg source imaging of anterior temporal lobe spikes: validity and reliability. *Clinical Neurophysiology*, *125*, 886–902.

Wennberg, R., Valiante, T., & Cheyne, D. (2011). Eeg and meg in mesial temporal lobe epilepsy: where do the spikes really come from? *Clinical neurophysiology*, *122*, 1295–1313.

Yamazaki, M., Tucker, D. M., Fujimoto, A., Yamazoe, T., Okanishi, T., Yokota, T., Enoki, H., & Yamamoto, T. (2012). Comparison of dense array eeg with simultaneous intracranial eeg for interictal spike detection and localization. *Epilepsy research*, *98*, 166–173.

Zumsteg, D., Friedman, A., Wieser, H. G., & Wennberg, R. A. (2006). Propagation of interictal discharges in temporal lobe epilepsy: correlation of spatiotemporal mapping with intracranial foramen ovale electrode recordings. *Clinical Neurophysiology*, *117*, 2615–2626.

Research Highlights:

- A Bayesian ESI technique is evaluated to localize interictal spike activity
- Averaged spikes in six patients were used that were seizure free after surgery
- We compared the technique with the LORETA an ECD technique
- We evaluated both spherical and 5-layered finite difference forward models
- Our approach is potentially useful to deliniate the irritative zone